Carbon and iron deficiencies in quiescent galaxies at z = 1–3 from JWST-SUSPENSE: implications for the formation histories of massive galaxies

Beverage, A.G.; Slob, M.M.; Kriek, M.T.; Conroy, C.; Barro, G.; Bezanson, R.; ... ; Weisz, D.R.

Citation

Beverage, A. G., Slob, M. M., Kriek, M. T., Conroy, C., Barro, G., Bezanson, R., … Weisz, D. R. (2025). Carbon and iron deficiencies in quiescent galaxies at z = 1–3 from JWST-SUSPENSE: implications for the formation histories of massive galaxies. *The Astrophysical Journal*, *979*(2). doi:10.3847/1538-4357/ad96b6

The Astrophysical Journal, 979:249 (15pp), 2025 February 1 https://doi.org/10.3847/1538-4357/ad96b6

Carbon and Iron Deficiencies in Quiescent Galaxies at $z = 1–3$ from JWST-SUSPENSE: Implications for the Formation Histories of Massive Galaxies

Aliza G. Beverage[1], Martje Slob[2], Mariska Kriek[2], Charlie Conroy[3], Guillermo Barro[4], Rachel Bezanson[5], Gabriel Brammer[6,7], Chloe M. Cheng[2], Anna de Graaff[8], Natascha M. Förster Schreiber[9], Marijn Franx[2], Brian Lorenz[1], Pavel E. Mancera Piña[2], Danilo Marchesini[10], Adam Muzzin[11], Andrew B. Newman[12], Sedona H. Price[5], Alice E. Shapley[13], Mauro Stefanon[14,15], Katherine A. Suess[18], Pieter van Dokkum[16], David Weinberg[17], and Daniel R. Weisz[1]

[1] Department of Astronomy, University of California, Berkeley, CA 94720, USA; abeverage@berkeley.edu
[2] Leiden Observatory, Leiden University, P.O. Box 9513, 2300 RA Leiden, The Netherlands
[3] Center for Astrophysics |Harvard & Smithsonian, Cambridge, MA 02138, USA
[4] Department of Physics, University of the Pacific, Stockton, CA 90340 USA
[5] Department of Physics and Astronomy and PITT PACC, University of Pittsburgh, Pittsburgh, PA 15260, USA
[6] Cosmic Dawn Center (DAWN), Denmark
[7] Niels Bohr Institute, University of Copenhagen, Jagtvej 128, DK2200 Copenhagen N, Denmark
[8] Max-Planck-Institut für Astronomie, Königstuhl 17, D-69117 Heidelberg, Germany
[9] Max-Planck-Institut für extraterrestrische Physik, Giessenbachstrasse 1, D-85748 Garching, Germany
[10] Department of Physics & Astronomy, Tufts University, MA 02155, USA
[11] Department of Physics and Astronomy, York University, 4700 Keele Street, Toronto, Ontario, ON MJ3 1P3, Canada
[12] Observatories of the Carnegie Institution for Science, 813 Santa Barbara Street, Pasadena, CA 91101, USA
[13] Department of Physics & Astronomy, University of California, Los Angeles, CA 90095, USA
[14] Departament d'Astronomia i Astrofísica, Universitat de València, C. Dr. Moliner 50, E-46100 Burjassot, València, Spain
[15] Unidad Asociada CSIC "Grupo de Astrofísica Extragaláctica y Cosmología," Instituto de Física de Cantabria,Universitat de València, Spain
[16] Astronomy Department, Yale University, 52 Hillhouse Avenue, New Haven, CT 06511, USA
[17] The Department of Astronomy and Center of Cosmology and AstroParticle Physics, The Ohio State University, Columbus, OH 43210, USA
[18] Department for Astrophysical & Planetary Science, University of Colorado, Boulder, CO 80309, USA

Received 2024 July 2; revised 2024 October 7; accepted 2024 October 21; published 2025 January 29

Abstract

We present the stellar metallicities and multielement abundances (C, Mg, Si, Ca, Ti, Cr, and Fe) of 15 massive ($\log M/M_\odot = 10.2–11.2$) quiescent galaxies at $z = 1–3$, derived from ultradeep JWST-SUSPENSE spectra. Compared to quiescent galaxies at $z \sim 0$, these galaxies exhibit a deficiency of 0.26 ± 0.04 dex in [C/H], 0.16 ± 0.03 dex in [Fe/H], and 0.07 ± 0.04 dex in [Mg/H], implying rapid formation and quenching before significant enrichment from asymptotic giant branch stars and Type Ia supernovae. Additionally, we find that galaxies forming at higher redshift consistently show higher [Mg/Fe] and lower [Fe/H] and [Mg/H], regardless of their observed redshift. The evolution in [Fe/H] and [C/H] is therefore primarily driven by lower-redshift samples naturally including galaxies with longer star formation timescales. In contrast, the lower [Mg/H] likely reflects earlier-forming galaxies expelling larger gas reservoirs during their quenching phase. Consequently, the mass–metallicity relation, primarily reflecting [Mg/H], is somewhat lower at $z = 1–3$ compared to the lower-redshift relation. Finally, we compare our results to standard stellar population modeling approaches employing solar abundance patterns and nonparametric star formation histories (using PROSPECTOR). Our simple stellar population (SSP)-equivalent ages agree with the mass-weighted ages from PROSPECTOR, while the metallicities disagree significantly. Nonetheless, the metallicities better reflect [Fe/H] than total [Z/H]. We also find that the star formation timescales inferred from elemental abundances are significantly shorter than those from PROSPECTOR, and we discuss the resulting implications for the early formation of massive galaxies.

Unified Astronomy Thesaurus concepts: Galaxy quenching (2040); Galaxy formation (595); Metallicity (1031); Chemical abundances (224)

1. Introduction

The chemical makeup of a galaxy is intimately linked to its past star formation, the amount of gas and stars it accretes, and the gas that is expelled through outflows. Consequently, the metal content of galaxies reflects fundamental physical processes that influence their evolution, such as star formation efficiency, feedback from massive stars and active galactic nuclei (AGN), and previous merger events. By characterizing how the metallicities of galaxies evolve across redshifts, we can obtain direct insights into the processes shaping galaxy growth throughout cosmic time.

In the nearby Universe, galaxies display a tight correlation between their stellar mass and metallicity, known as the mass–metallicity relation (MZR; e.g., J. Lequeux et al. 1979; C. A. Tremonti et al. 2004; A. Gallazzi et al. 2005; E. N. Kirby et al. 2013). For star-forming galaxies, the gas-phase MZR has been routinely studied out to $z \sim 3$ mostly using strong-line indicators (e.g., R. Maiolino et al. 2008; H. J. Zahid et al. 2013; R. L. Sanders et al. 2020, 2021; C. Papovich et al. 2022; A. E. Shapley et al. 2023) and has recently been confirmed up to $z \sim 8$ with the advent of JWST (D. Langeroodi et al. 2023; K. Nakajima et al. 2023; M. Curti et al. 2024). Quiescent galaxies, however, lack the strong emission lines needed for gas-phase measurements, so we instead rely on faint absorption lines originating from stellar atmospheres. At higher redshifts, measuring stellar metallicity becomes increasingly challenging as key absorption features shift to near-infrared (NIR) wavelengths, where ground-based spectroscopic observations are severely hindered by skylines. As a result, the MZR of quiescent galaxies has only been systematically studied up to $z \sim 0.7$, showing little evolution since $z \sim 0$ (J. Choi et al. 2014; A. Gallazzi et al. 2014; T. M. Barone et al. 2022; A. G. Beverage et al. 2023).

Beyond $z \sim 1$, the picture is much less clear. Currently, there is only a handful of stellar metallicity measurements of quiescent galaxies at $z = 1$–2.2 based on absorption lines, mostly relying on methods such as spectral stacking (M. Onodera et al. 2015; A. C. Carnall et al. 2022), observations of rare lensed massive galaxies (M. Jafariyazani et al. 2020; A. W. S. Man et al. 2021; M. Akhshik et al. 2023; Z. Zhuang et al. 2023; M. Jafariyazani et al. 2024), low-resolution spectroscopy (T. Morishita et al. 2018; V. Estrada-Carpenter et al. 2019; M. Akhshik et al. 2023), or utilizing extreme integration times on the most efficient ground-based telescopes (M. Kriek et al. 2016, 2019; A. G. Beverage et al. 2024; M. Kriek et al. 2024). Despite the small samples at these redshifts, there is a growing consensus that massive quiescent galaxies at $z \gtrsim 1$ exhibit significantly lower [Fe/H] compared to their present-day counterparts (e.g., M. Kriek et al. 2019; Z. Zhuang et al. 2023; A. G. Beverage et al. 2024). There are, however, a couple of conflicting findings, with two studies reporting exceptionally high metallicities comparable to the most metal-rich galaxies at $z \sim 0$ (I. Lonoce et al. 2015; M. Jafariyazani et al. 2020). These contrasting results may not be surprising, given that the uncertainties in individual measurements remain high, and the methods vary significantly between studies (e.g., I. Lonoce et al. 2015; M. Onodera et al. 2015; M. Kriek et al. 2016; V. Estrada-Carpenter et al. 2019; P. Saracco et al. 2023).

Understanding the metallicities of distant quiescent galaxies is crucial, as they hold significant implications for the enrichment, star formation timescales, quenching, and assembly of galaxies across cosmic time. Specifically, the multielement abundance patterns provide direct insight into the star formation histories (SFHs) of galaxies. Such insight is largely owed to the diverse enrichment timescales of the elements. α elements (e.g., O and Mg) are instantaneously released by core-collapse supernovae (CC SNe). C and N are released approximately equally by CC SNe and by the winds of low-mass asymptotic giant branch (AGB) stars, which only contribute after a characteristic delay time of ~250 Myr (e.g., S. Cristallo et al. 2011, 2015; R. Maiolino & F. Mannucci 2019; J. W. Johnson et al. 2023). Fe-peak elements are enriched by both CC SNe and the explosions of intermediate-mass stars (Type Ia SNe (SNe Ia)), which occur only after a longer delay (of ~1 Gyr; D. Maoz et al. 2010).

To fully exploit chemical compositions for understanding the formation histories of massive galaxies, we need a larger sample of massive quiescent galaxies at $z \gtrsim 1$ with deep spectra covering multiple absorption features. Such observations are now finally possible with JWST. To that end, we have conducted the JWST-SUSPENSE program, an ultradeep rest-frame optical spectroscopic NIRSpec/ microshutter assembly (MSA) survey of 20 massive quiescent galaxies at $z = 1$–3 (M. Slob et al. 2024).

In this paper, we present the metallicities and multielement abundances of distant quiescent galaxies at $z = 1$–3 from the JWST-SUSPENSE survey. In Section 2 we describe the observations and elemental abundance analysis, in Section 3 we present the abundance results, in Section 4 we present the MZR at $z = 1$–3, and in Section 5 we discuss the implications of the results on star formation timescales, the assembly of massive galaxies, and star formation quenching. In Section 5 we also compare the full-spectrum modeling results to those from PROSPECTOR and discuss the implications of this comparison on the early formation of massive galaxies. In Section 6, we present a summary. Throughout this paper, we assume a P. Kroupa (2001) initial mass function (IMF), solar abundances from M. Asplund et al. (2009), and a flat Lambda cold dark matter (ΛCDM) cosmology with $\Omega_{\rm m} = 0.3$ and $H_0 = 70$ km s^{-1} Mpc^{-1}.

2. Observations and Analysis

All galaxies in this study are drawn from the JWST-SUSPENSE Program (ID: 2110) which obtained ultradeep (16.4 hr) NIRSpec/MSA/G140M-F100LP observations of a sample of 20 massive quiescent galaxies at $z = 1$–3 (M. Slob et al. 2024). The spectroscopic observations were reduced using a modified version of the JWST Science Calibration Pipeline (H. Bushouse et al. 2023) v1.12.5, and version 1183 of the Calibration Reference Data System (see M. Slob et al. 2024, for details). Primary targets were initially identified using the UltraVISTA *K*-band selected Data Release 3 (DR3) catalog (A. Muzzin et al. 2013a) and selected to be quiescent using the *UVJ* criterion from A. Muzzin et al. (2013b). The targets represent the general population of quiescent galaxies at $z = 1$–3, encompassing the full quiescent range in *UVJ* space at these redshifts, and are all confirmed to have quiescent stellar populations (see M. Slob et al. 2024).

The observations cover wavelengths from 0.97 to 1.84 μm, corresponding to a typical rest-frame range of approximately 3700 to 7000 Å. Most objects have coverage of the Mg b line, several prominent Fe features, and multiple Balmer lines. The stellar masses and star formation rates (SFRs) were derived by M. Slob et al. (2024) by fitting the spectra and photometry simultaneously with PROSPECTOR (J. Leja et al. 2019a; B. D. Johnson et al. 2021) assuming a G. Chabrier (2003) IMF. They consider two nonparametric SFH models: a fixed-bin model (J. Leja et al. 2019a) and a poststarburst model (K. A. Suess et al. 2022a). For more details on target selection, observing strategy, data reduction, redshift determination, and stellar population properties we refer to M. Slob et al. (2024).

We measure the individual elemental abundances and stellar population ages using the custom full-spectrum fitting code `alfα` (A. Beverage 2024)[19] based on the `alf` fitting code presented in C. Conroy et al. (2018). The C. Conroy et al. (2018) models were developed to measure the elemental abundance patterns of old ($\gtrsim$1 Gyr) stellar populations. They combine metallicity-dependent MIST isochrones (J. Choi et al. 2016), empirical MILES and IRTF spectral libraries (P. Sanchez-Blazquez et al. 2006; A. Villaume et al. 2017), and synthetic metallicity- and age-dependent elemental response spectra for 19 elements.

The models assume a single burst of star formation a simple stellar population (SSP) and a P. Kroupa (2001) IMF. We fit for

---

[19] https://github.com/alizabeverage/alfalpha

a total of 20 free parameters: velocity offset, velocity dispersion, single SSP-equivalent stellar population age, isochrone metallicity, 10 individual elemental abundances (Fe, C, N, Mg, Na, Si, Ca, Ti, and Cr), Balmer emission line flux, the emission line velocity and broadening, a shift in the effective temperature of the fiducial isochrones ($T_{\rm eff}$), and an instrumental jitter term to account for under-/overestimation of the uncertainties. The abundance ratios of the other nine elements are fixed to solar ($[{\rm X/Fe}] = 0$) following the results of the mock-recovery test presented in A. G. Beverage et al. (2023). We use the `dynesty` dynamic nested sampling package (J. S. Speagle 2020) to sample the posterior distributions of the 20 parameters.

Before fitting, we smooth the models to the instrumental resolution of the observations. We derive the instrumental resolution as a function of wavelength in the raw spectral frames using `msafit` (A. de Graaff et al. 2024). We provide `msafit` with the morphology of each galaxy, its position and angle with respect to the MSA slit, and a spectrum filled with equally spaced delta functions that simulate idealized emission lines. The software then simulates a 2D spectrum for each object. We process these 2D spectra using the JWST NIRSpec reduction pipeline in the same manner as the actual data. Finally, we measure the spectral resolution by analyzing the broadening of the simulated emission lines. We find that the wavelength dependence of the instrumental resolution is consistent with the online prelaunch estimates from JDox, but typically a factor of 1.3 better, corresponding to a resolution of $R \sim 1300$. For each galaxy, we derive this factor and assume the corrected JDox curve when fitting. See M. Slob et al. (2024) for more details on this procedure.

During the fitting procedure, the spectral continuum is removed from the observations by fitting an $n = 7$ Chebyshev polynomial to the ratio of the data to the model. We note that the results are robust to decisions regarding the order of the polynomial. Where available, we fit the wavelength regions 3800–4800 Å, 4800–5800 Å, 5800–6400 Å, and 8000–8600 Å (each with their own normalized continuum). We mask the Na D absorption feature, the [O III] lines where present, and the Hα + [N II] complex. We also exclude wavelengths 6400–8000 Å due to the dominant TiO absorption in the spectrum, as these broad features are typically overfitted by the continuum polynomial.

After fitting all 20 galaxies, we visually inspect the best-fit model, the normalizing polynomial, and the corresponding corner plots. We remove five galaxies; two because they have low signal-to-noise ratio (S/N; <15 per rest-frame Å; IDs: 130183 and 130934), one because it is lacking wavelength coverage of key absorption features (130208), and two because of strong emission lines likely associated with AGN (130647 and 128452). We also refit 127941, masking the Hβ region, which was poorly fit due to spectral contamination. Object 127108 is also refit, masking the region >5500 Å due to the lack of clear features. Finally, for each object, we inspect the posteriors of all 10 fitted elements and determine which elements can be constrained by requiring their posterior to be Gaussian and not run against the prior limits (−0.5 and 0.5 dex). Figure 1 shows the quiescent SUSPENSE spectra at $z = 1$–3 and corresponding best-fit `alfα` models. We present the stellar population properties and elemental abundances [X/H] in Table 1. The elements flagged as "poorly constrained" during the visual inspection are omitted from Table 1. We also omit the abundances of 129966 because the best-fit age is below the lowest age in the stellar population models (1 Gyr). Tables of the elemental abundance ratios [X/Fe] and [X/Mg] are provided in the Appendix.

3. The Multielemental Abundances of Distant Quiescent Galaxies

In this section, we present the multielement abundances of the massive quiescent galaxies at $z = 1$–3 from the JWST-SUSPENSE program. For each SUSPENSE galaxy, we only consider the elements that have well-behaved normal posterior distributions. Among the 10 fitted elements, C, Mg, and Fe have the most galaxies with well-constrained measurements, likely due to their prominent absorption features, such as CH (G4300), Mg b, Fe λ5270, Fe λ5335, and Fe λ5406.

In Figure 2, we present the formation time ($t_{\rm form}$), [Fe/H], [Mg/H], [Fe/Mg], and [C/Mg] as a function of line-of-sight velocity dispersion (circles). Here, we adopt Mg as the reference element instead of Fe (i.e., [X/Mg]) because it is mostly produced by CC SNe and thus a simpler tracer of chemical enrichment (see, e.g., D. H. Weinberg et al. 2019). The formation time is calculated using the stellar ages from Table 1, corrected for the age of the Universe at the observed redshift. The points are colored by their spectroscopic redshifts. We also include the results of stacked quiescent galaxies at $z \sim 0$ from the Sloan Digital Sky Survey (SDSS; red squares) and $z \sim 0.7$ from LEGA-C (pink triangles; A. G. Beverage et al. 2023). The stacked SDSS spectra and corresponding elemental abundance results were first presented in C. Conroy et al. (2014) and later refit by A. G. Beverage et al. (2023) to reflect updates in the stellar population models (see C. Conroy et al. 2018). We note that the SDSS fiber and the LEGA-C and SUSPENSE slits all cover similar physical radii (3–4 kpc). However, since galaxies were smaller in the past, the SUSPENSE and LEGA-C slits cover 1–1.2 R_e, while SDSS covers only 0.4–0.8 R_e.

In Figure 2, we also include all available elemental abundance measurements in the literature at $z = 1$–3. We only include measurements that use the same full-spectrum fitting method, and thus are comparable to the SUSPENSE results. We do not include grism or prism results because they rely heavily on the shape of the continuum and are therefore highly susceptible to fitting degeneracies. We also exclude abundances derived from Lick indices because, at these redshifts, the individual absorption features are faint and easily contaminated by NIR skylines. We color all points by their spectroscopic redshifts.

In each panel of Figure 2, we present the results from a linear structural regression fit applied to all available points within the redshift range $z = 1$–3. The linear model assumes intrinsic scatter around the best-fit line, which is described by a third parameter alongside the slope and intercept. Using a Bayesian approach, we determine the best-fit line and its associated shaded confidence intervals by sampling the posterior distributions with Markov Chain Monte Carlo (MCMC). We fit two relations to the formation times, one at $z < 1.7$ (light blue) and another at $z > 1.7$ (dark blue). During the fitting process, we set a lower limit of 0.1 dex on the uncertainties of the elemental abundance, to prevent single high S/N measurements from dominating the fit and to account for possible systematic uncertainties.

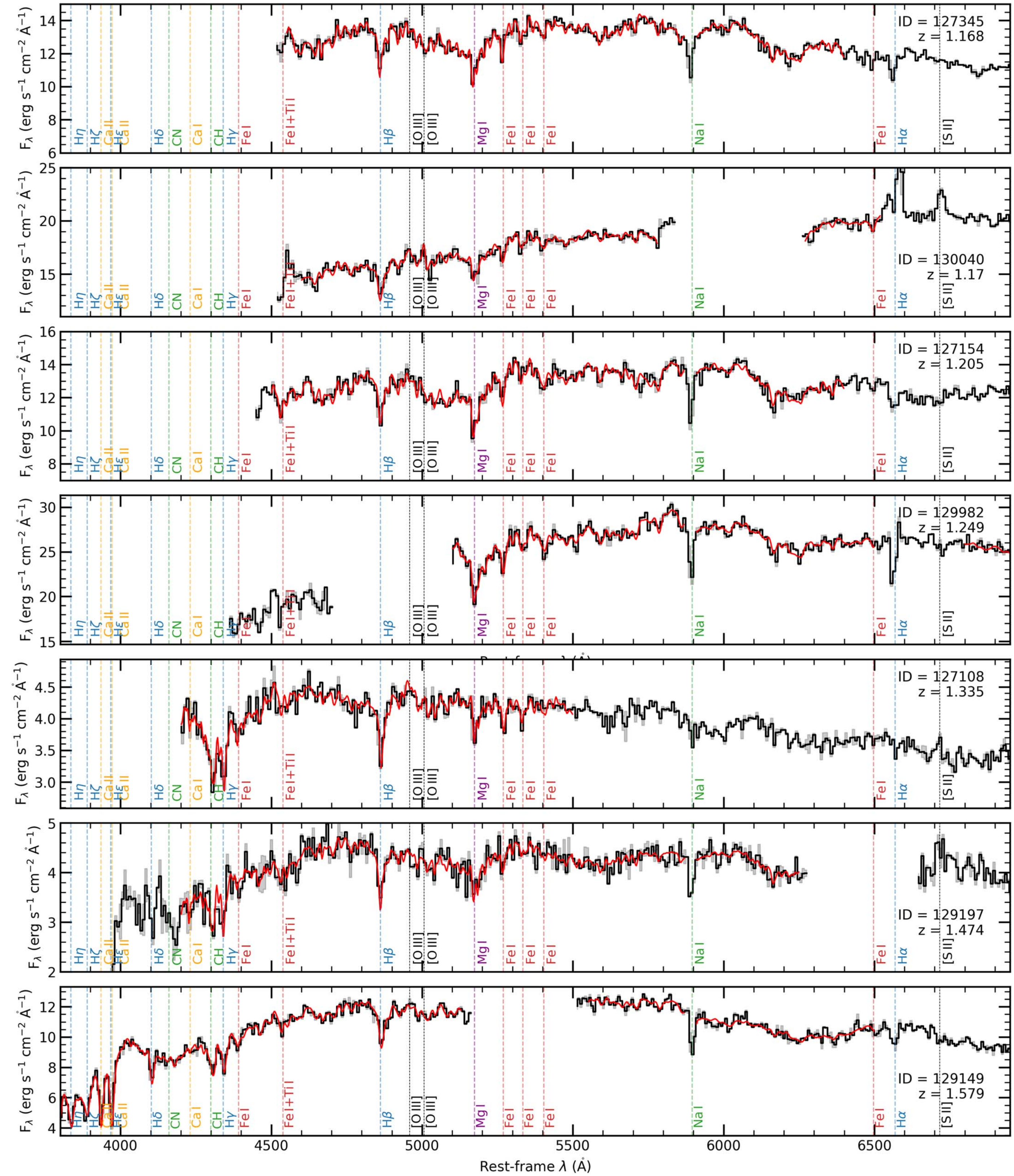

Figure 1. JWST-SUSPENSE spectra of quiescent galaxies at $z = 1$–3 (black) and corresponding 1σ uncertainties (gray). The best-fit stellar population models are shown in red. The wavelength array has been corrected for redshift and is shown in the rest frame. The spectra have been median binned by 3 pixels (8 Å in the rest frame).

In the top left panel of Figure 2, we find that the formation redshifts of the SUSPENSE galaxies range from $z_{\rm form} = 1.5$ to 9. No clear trends are observed between σ and formation time at $z \gtrsim 1$. However, there is a clear trend with observed redshift, where typical galaxies at $z \gtrsim 1$ formed earlier than those at lower redshifts, as expected. This redshift trend is also evident

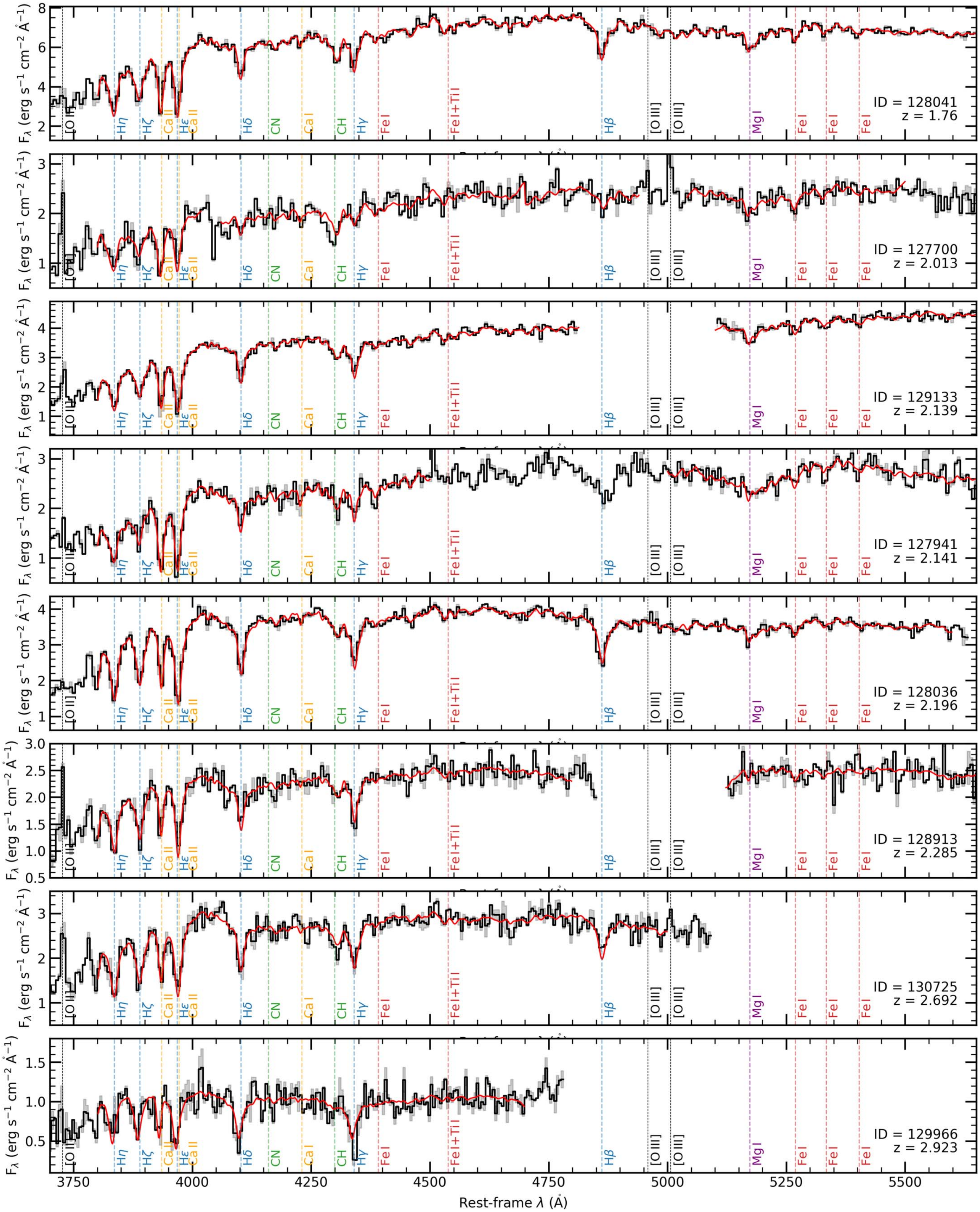

Figure 1. (Continued.)

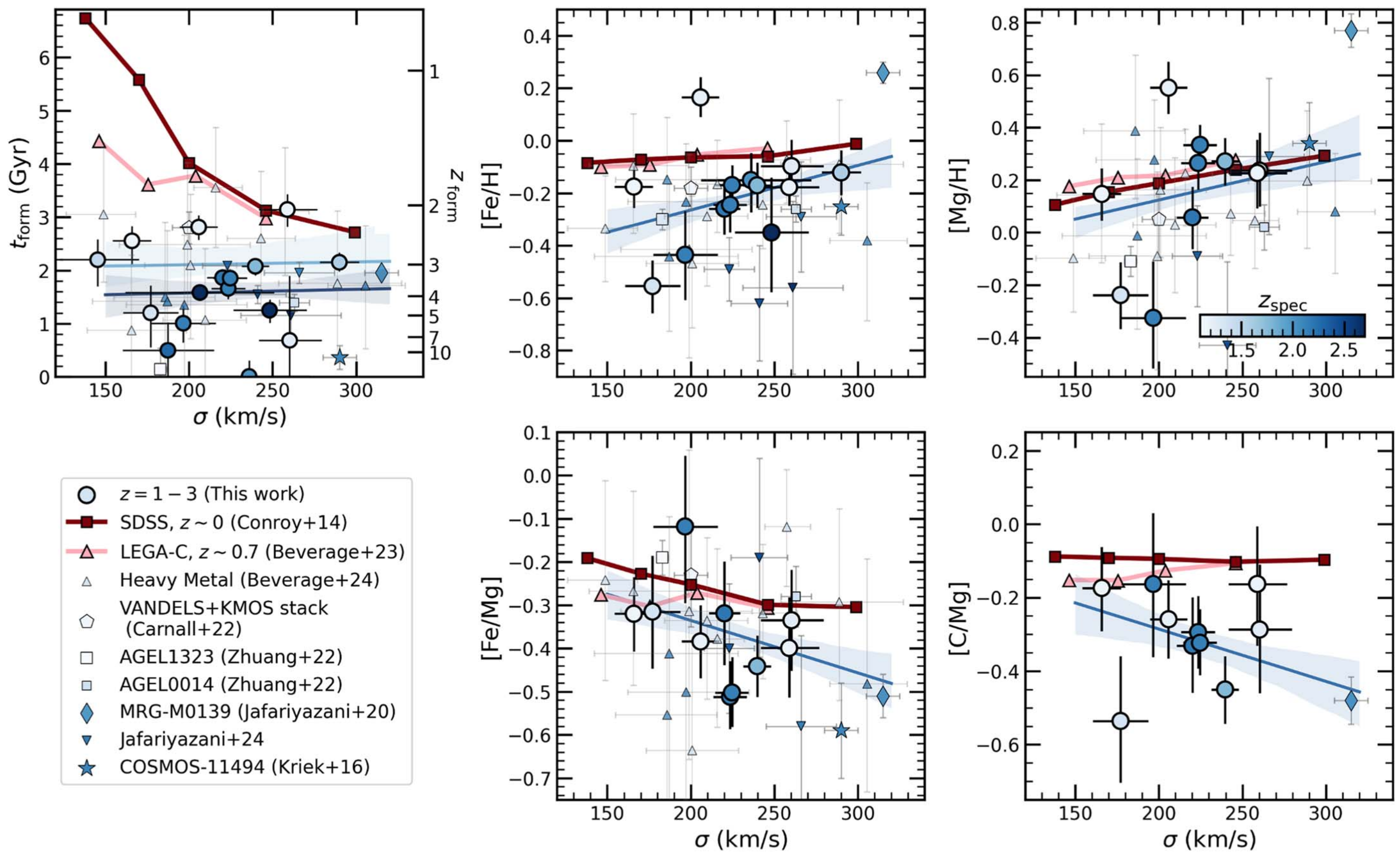

Figure 2. The formation time ($t_{\rm form}$), [Fe/H], [Mg/H], [Fe/Mg], and [C/Mg] as a function of velocity dispersion for the $z = 1$–3 JWST-SUSPENSE quiescent galaxy sample (circles) and for other various measurements at similar redshifts from the literature. Each point is colored by its spectroscopic redshift. To guide the eye, we include the best-fit relations and corresponding confidence intervals in each panel, fit to the $z = 1$–3 data point. In the $t_{\rm form}$ panel, we instead present two relations, one for $z < 1.5$ and the other for $z > 1.5$. For comparison, we also include the abundances of stacks of quiescent galaxies at $z \sim 0$ from SDSS (C. Conroy et al. 2014; A. G. Beverage et al. 2023) and at $z \sim 0.7$ from LEGA-C (A. G. Beverage et al. 2023). At constant σ, the SUSPENSE galaxies form earlier and are more deficient in Fe and C than the $z < 0.7$ galaxies.

Table 1

JWST-SUSPENSE Stellar Population Parameters

ID	$z_{\rm spec}$[a]	log M[a] ($M_\odot$)	σ (km s^{-1})	Age (Gyr)	[Fe/H]	[Mg/H]	[C/H]	[Ca/H]	[Ti/H]	[Cr/H]	[Si/H]
127345	1.168	10.7	166^{+11}_{-12}	$2.6^{+0.4}_{-0.3}$	$-0.17^{+0.08}_{-0.08}$	$0.15^{+0.10}_{-0.10}$	$-0.03^{+0.09}_{-0.10}$	$0.14^{+0.09}_{-0.08}$	…	$-0.19^{+0.12}_{-0.12}$	$-0.10^{+0.12}_{-0.13}$
130040	1.170	11.2	259^{+18}_{-17}	$2.0^{+0.3}_{-0.3}$	$-0.18^{+0.08}_{-0.07}$	$0.23^{+0.13}_{-0.13}$	$0.07^{+0.13}_{-0.15}$	$-0.04^{+0.11}_{-0.11}$	$0.38^{+0.19}_{-0.23}$	$0.04^{+0.17}_{-0.16}$	$-0.07^{+0.14}_{-0.13}$
127154	1.205	10.7	206^{+11}_{-11}	$2.2^{+0.2}_{-0.2}$	$0.17^{+0.08}_{-0.08}$	$0.55^{+0.10}_{-0.10}$	$0.30^{+0.07}_{-0.09}$	…	$0.47^{+0.14}_{-0.16}$	$0.06^{+0.13}_{-0.13}$	$0.39^{+0.10}_{-0.11}$
129982	1.249	11.2	260^{+19}_{-18}	$4.2^{+1.3}_{-1.2}$	$-0.10^{+0.10}_{-0.10}$	$0.24^{+0.14}_{-0.14}$	$-0.05^{+0.16}_{-0.16}$	$0.04^{+0.12}_{-0.14}$	$0.06^{+0.21}_{-0.21}$	$0.19^{+0.16}_{-0.16}$	…
127108	1.335	10.2	177^{+17}_{-16}	$3.4^{+0.6}_{-0.5}$	$-0.55^{+0.10}_{-0.10}$	$-0.24^{+0.12}_{-0.13}$	$-0.77^{+0.14}_{-0.14}$	$-0.61^{+0.19}_{-0.18}$	…	$-0.95^{+0.14}_{-0.13}$	$-0.23^{+0.18}_{-0.23}$
129197	1.474	10.5	145^{+25}_{-23}	$2.1^{+0.5}_{-0.4}$	…	…	…	…	…	…	…
129149	1.579	11.0	290^{+12}_{-12}	$1.9^{+0.2}_{-0.2}$	$-0.12^{+0.08}_{-0.09}$	…	$0.01^{+0.10}_{-0.11}$	$-0.19^{+0.07}_{-0.07}$	$0.23^{+0.15}_{-0.18}$	$0.06^{+0.16}_{-0.15}$	$-0.01^{+0.16}_{-0.18}$
128041	1.760	10.7	240^{+8}_{-8}	$1.6^{+0.2}_{-0.1}$	$-0.17^{+0.09}_{-0.09}$	$0.27^{+0.09}_{-0.09}$	$-0.18^{+0.10}_{-0.11}$	$-0.12^{+0.06}_{-0.06}$	$0.17^{+0.12}_{-0.13}$	$-0.27^{+0.12}_{-0.12}$	$-0.21^{+0.12}_{-0.14}$
127700	2.013	10.9	236^{+36}_{-30}	$3.2^{+0.2}_{-0.3}$	$-0.15^{+0.10}_{-0.12}$	…	$-0.24^{+0.14}_{-0.15}$	$-0.18^{+0.11}_{-0.11}$	…	…	…
129133	2.139	11.1	223^{+10}_{-10}	$1.4^{+0.2}_{-0.2}$	$-0.24^{+0.10}_{-0.11}$	$0.27^{+0.10}_{-0.10}$	$-0.03^{+0.13}_{-0.14}$	$0.18^{+0.06}_{-0.06}$	…	$-0.21^{+0.15}_{-0.17}$	$-0.00^{+0.16}_{-0.19}$
129133	2.139	11.1	225^{+10}_{-10}	$1.2^{+0.1}_{-0.1}$	$-0.17^{+0.08}_{-0.08}$	$0.33^{+0.08}_{-0.09}$	$0.01^{+0.09}_{-0.09}$	$0.22^{+0.06}_{-0.06}$	…	$-0.14^{+0.15}_{-0.14}$	$0.07^{+0.14}_{-0.15}$
127941	2.141	10.8	197^{+20}_{-19}	$2.0^{+0.4}_{-0.3}$	$-0.43^{+0.17}_{-0.17}$	$-0.33^{+0.22}_{-0.19}$	$-0.48^{+0.21}_{-0.21}$	$0.18^{+0.10}_{-0.10}$	…	$0.07^{+0.21}_{-0.22}$	$0.01^{+0.18}_{-0.22}$
128036	2.196	10.9	220^{+9}_{-9}	$1.1^{+0.1}_{-0.1}$	$-0.26^{+0.09}_{-0.10}$	$0.06^{+0.12}_{-0.12}$	$-0.27^{+0.11}_{-0.12}$	$0.15^{+0.05}_{-0.05}$	…	$-0.45^{+0.18}_{-0.18}$	$-0.25^{+0.18}_{-0.21}$
128913	2.285	10.9	187^{+28}_{-27}	$2.3^{+0.5}_{-0.5}$	…	…	…	…	…	…	…
130725	2.692	11.1	248^{+22}_{-22}	$1.1^{+0.2}_{-0.2}$	$-0.35^{+0.21}_{-0.23}$	…	…	$-0.09^{+0.12}_{-0.13}$	…	…	…
129966[b]	2.923	10.9	207^{+44}_{-45}	$0.6^{+0.1}_{-0.1}$	…	…	…	…	…	…	…

Notes.

[a] Presented in M. Slob et al. (2024).

[b] Removed from analysis because younger than the stellar population model grid (<1 Gyr).

within the $z \gtrsim 1$ sample, with the best-fit relation for $z > 1.7$ being lower than that for $z < 1.7$. A similar trend has been shown by A. G. Beverage et al. (2023) and will be discussed in detail in Section 5.2.

In the next panel, we show that quiescent galaxies at $z = 1$–3 have [Fe/H] ranging from −0.6 to 0.3, with typical values of −0.22. We find a trend between σ and [Fe/H], with a statistically significant slope (2σ certainty). The normalization of these measurements are 0.16 ± 0.03 dex lower than what is found at $z \sim 0$ and $z \sim 0.7$. A 1D Kolmogorov–Smirnov (K-S) test comparing the Fe abundances of galaxies at $z \sim 0$ and $z \sim 2$ yields significant p-values (<0.01), allowing us to reject the null hypothesis and conclude that the Fe abundances of these two populations are drawn from different distributions. Thus, we confirm earlier results that quiescent galaxies at $z \sim 2$ are Fe deficient (M. Kriek et al. 2016; T. Morishita et al. 2018; M. Kriek et al. 2019; Z. Zhuang et al. 2023; A. G. Beverage et al. 2024; M. Jafariyazani et al. 2024). In the next panel, we find that [Mg/H] varies from −0.3 to 0.6, with a typical value of [Mg/H] = 0.15. The slope of the σ–[Mg/H] relation agrees with the results at $z \sim 0$ and $z \sim 0.7$ and the normalization is only slightly lower (0.07 ± 0.04 dex).

In the bottom left panel of Figure 2 we find [Fe/Mg] ranging from −0.50 to −0.10, with a typical value of −0.35. The best-fit σ–[Fe/Mg] relation has a negative slope, in agreement with lower-redshift results, however, the relation is offset to lower [Fe/Mg] by 0.10 ± 0.04 dex. A 1D K-S test of [Fe/Mg] show that the $z \sim 0$ and $z \sim 2$ abundances are drawn from different distributions, with a mildly significant p-value (<0.05). This low [Fe/Mg] is consistent with the other results at similar redshifts in this figure (M. Kriek et al. 2016; M. Jafariyazani et al. 2020; A. G. Beverage et al. 2024; M. Jafariyazani et al. 2024).

In the bottom right panel, we show [C/Mg]. We highlight that these are the first measurements of C abundances for a sample of distant quiescent galaxies and that only one other [C/Mg] measurement at these redshifts is available in the literature (M. Jafariyazani et al. 2020). We find [C/Mg] ranges from −0.55 to −0.05, with a typical value of −0.3, in good agreement with M. Jafariyazani et al. (2020). The best-fit trend with σ is still highly uncertain given that there are only 10 C measurements at this redshift but it is clear that the SUSPENSE galaxies have ∼0.2 dex lower [C/Mg] than the $z \sim 0$ and $z \sim 0.7$ samples (3σ certainty). Given that the average [Mg/H] is similar (to within 0.07 dex) across the redshift samples, the low [C/Mg] and [Fe/Mg] are caused by deficiencies in C and Fe.

Next, we present the elemental abundance patterns of the SUSPENSE galaxies in Figure 3. We show the average absolute abundances [X/H] (top panel), the abundance ratios with respect to Fe [X/Fe] (middle panel), and the abundance ratios with respect to Mg [X/Mg] (bottom panel). We only include elements for which we have at least five constrained individual measurements, namely C, Mg, Si, Ca, Ti, and Cr, and Fe. The small blue squares represent the individual abundances from SUSPENSE, while the large squares depict the mean of these measurements. The black error bars are calculated by perturbing the abundance of each data point based on the uncertainty and then determining the standard deviation of the resulting mean abundance values. Figure 3 also includes the abundance patterns of $z \sim 0$ (red circles) and $z \sim 0.7$ quiescent galaxies (pink triangles) from A. G. Beverage et al. (2023). These $z \sim 0$ [$z \sim 0.7$] results represent the average of thousands [hundreds] of quiescent galaxies from the same velocity dispersion range as the SUSPENSE galaxies (200–300 km s^{-1}).

Consistent with the findings of Figure 2, massive quiescent galaxies at all three redshift intervals have nonsolar abundance patterns, being deficient with respect to Mg. These trends are further evident when examining the individual elements in greater detail. In the top panel of Figure 3, we find that distant quiescent galaxies in SUSPENSE have significantly lower [C/H] and [Fe/H] (>3σ certainty) and slightly lower [Mg/H] (1.5σ) than the $z < 1$ galaxies. Specifically, [C/H], [Fe/H], and [Mg/H] are lower by 0.25, 0.16, and 0.07 dex, respectively, than at $z \sim 0$. Therefore, the [Mg/Fe] enhancement observed in the central panel is primarily driven by a deficiency in Fe. Moving on to the other elements, we find that Ca has a similar behavior as Mg, with a mostly constant [Ca/H] across the three redshift regimes, but with enhanced [Ca/Fe] and [Ca/Mg] at higher redshift. Ti is unique because the absolute abundance [Ti/H] and abundance ratios [Ti/Fe] and [Ti/Mg] increase with increasing redshift. We highlight that high Ti abundances present a long-standing problem in chemical evolution modeling (e.g., C. Kobayashi et al. 2020). [Cr/H] on the other hand behaves more like Fe and C, with [Cr/H] being lower at $z = 1$–3. This result is unsurprising given that Cr is typically considered an Fe-peak element. Si shows no significant evolution in [X/H], [X/Fe], or [X/Mg]. Thus, Si behaves more similarly to Mg and Ca. However, the abundance uncertainties on Ti, Si, and Cr are quite large. We note that these abundance results are roughly consistent with the only other existing abundance pattern at $z \gtrsim 0.7$, observed in a lensed quiescent galaxy by M. Jafariyazani et al. (2020). In Section 5.1, we explore the implications of these abundance patterns in the context of chemical enrichment histories.

Finally, in Figure 4, we show [Fe/H], [Mg/H], and [Mg/Fe] as a function of formation time, as in Z. Zhuang et al. (2023). In addition to the SUSPENSE sample (blue circles, colored by spectroscopic redshift), we include individual results from massive quiescent galaxies in the SDSS survey from Z. Zhuang et al. (2023, red circles) and LEGA-C from A. G. Beverage et al. (2023, pink triangles). In each panel of Figure 4, we remove the first-order dependence on stellar mass by subtracting the SDSS M_*–abundance relations from Z. Zhuang et al. (2023) from all galaxies and then scaling them to the value of the M_*–abundance relations at $M_* = 10^{11}\ M_\odot$. We utilize the Pearson correlation coefficient to assess the degree of correlation between the parameters in Figure 4. We include all points in Figure 4 (at all redshifts) when computing the degree of correlation. The resulting Pearson coefficients and corresponding p-values are listed in the top left of each panel. Correlations with p-values of $p < 0.01$ are considered significant.

At fixed stellar mass, the formation time and [Fe/H] have a significant positive correlation ($r = 0.59$), with galaxies forming at earlier times having lower Fe enrichment. [Mg/H] shows a moderate positive correlation ($r = 0.30$), with galaxies forming earlier having slightly lower Mg enrichment. Finally, there is a negative correlation ($r = -0.40$) between [Mg/Fe] and formation time, indicating galaxies that form earlier have slightly higher [Mg/Fe]. These correlations are primarily driven by the large quantity and dynamic range in $t_{\rm form}$ of $z \sim 0$ abundance measurements and thus agree with the results

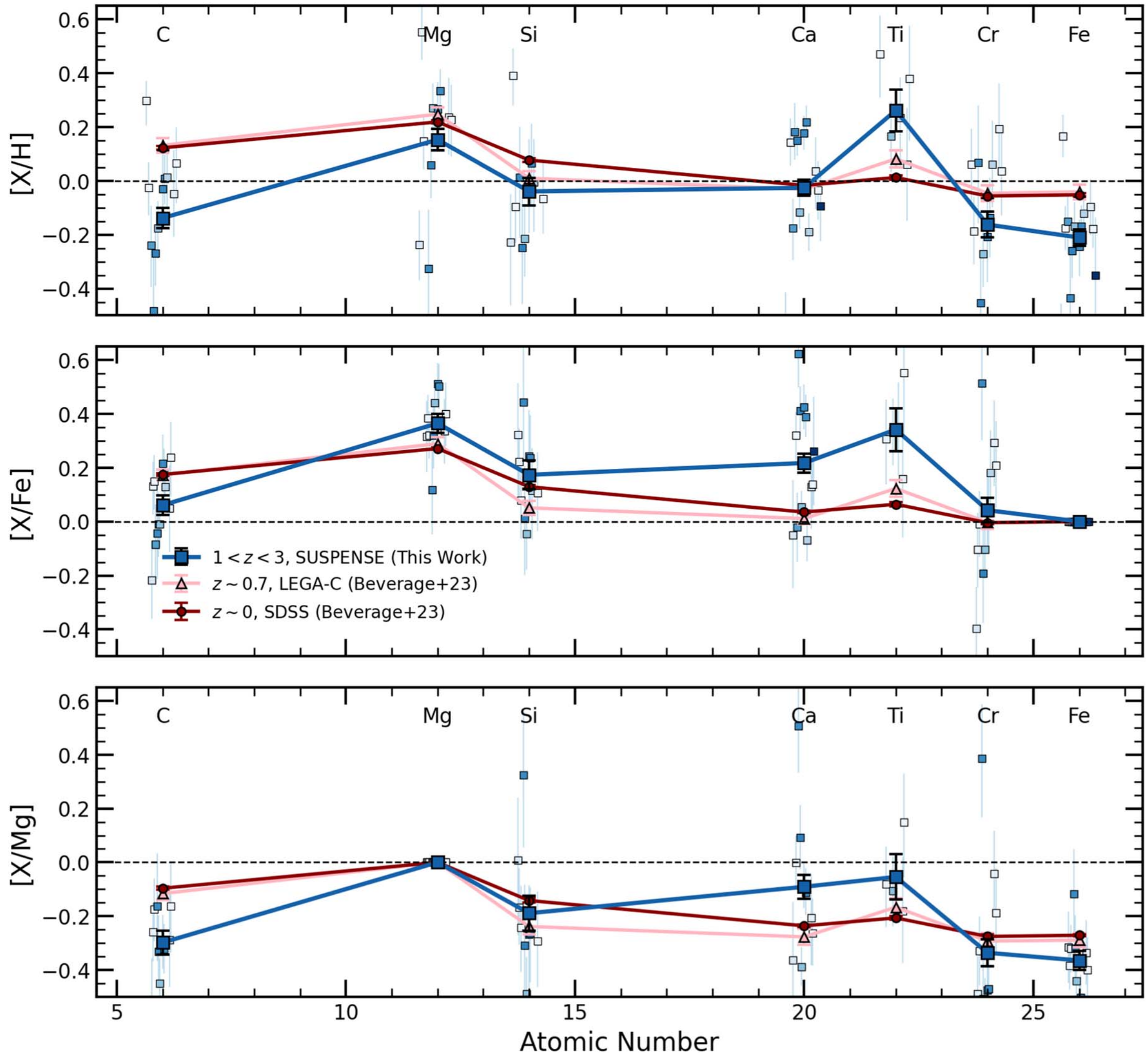

Figure 3. The abundance patterns of the $z = 1$–3 quiescent galaxies (blue squares). We show the absolute abundances, [X/H], in the top panel, followed by the abundance ratios [X/Fe] (middle) and [X/Mg] (bottom), with the solar values marked with a dashed black line. The thick solid blue line with square markers shows the median abundance pattern of the $z = 1$–3 quiescent galaxies. For comparison, we include the average abundance patterns of $z \sim 0$ (red solid line with circle markers) and $z \sim 0.7$ (pink solid line with triangle markers) galaxies with the same velocity dispersions (175–275 km s^{-1}). The $z = 1$–3 galaxies are significantly deficient in [C/H] and [Fe/H] compared to lower-redshift samples.

presented in Z. Zhuang et al. (2023). Therefore, it is striking that the correlations found at lower redshifts are mostly consistent with the $z \sim 2$ data, in the sense that the oldest galaxies at $z \sim 0$ have similar abundance patterns as those at $z \sim 2$. In Section 5.2, we discuss the implications of these results on the assembly of massive galaxies.

4. The Stellar Mass–Metallicity Relation at $z \sim 2$

In this section, we present the stellar MZR of quiescent galaxies at $z = 1$–3. In Figure 5, we show the stellar metallicities $\log(Z/Z_\odot)$ of the JWST-SUSPENSE quiescent galaxies as a function of their stellar mass (circles). We compute these metallicities following the calibration $\log(Z/Z_\odot) = [\mathrm{Fe/H}] + 0.94[\mathrm{Mg/Fe}]$ from D. Thomas et al. (2003). As in Figure 2, we include all existing measurements of stellar metallicities derived from full-spectrum fitting at $z = 1$–3 derived using the same full-spectrum fitting method and underlying models. For comparison, we also include the $z \sim 0$ MZR and corresponding 1σ scatter from A. Gallazzi et al. (2005, black line and gray shaded region). Additionally, we show individual measurements for a subsample of these SDSS galaxies from Z. Zhuang et al. (2023, gray hexagons). The A. Gallazzi et al. (2005) relation was measured using a different method than Z. Zhuang et al. (2023), with different stellar population models, and assuming a different solar abundance pattern. Therefore, we calibrate the A. Gallazzi et al. (2005) MZR to match the normalization of the Z. Zhuang et al. (2023) measurements by applying a shift of +0.16 dex.

We fit an MZR to all available $z = 1$–3 measurements using the same structural linear regression applied to the abundances in Figure 2, where we assume that the points have an intrinsic scatter around the best-fit line. Again, we set the lower limit on the error of the metallicity to 0.1 dex so that high S/N measurements do not dominate the fit. Uncertainties on all stellar mass estimates are assumed to be 0.1 dex, to properly account for systematic uncertainties involved in the stellar

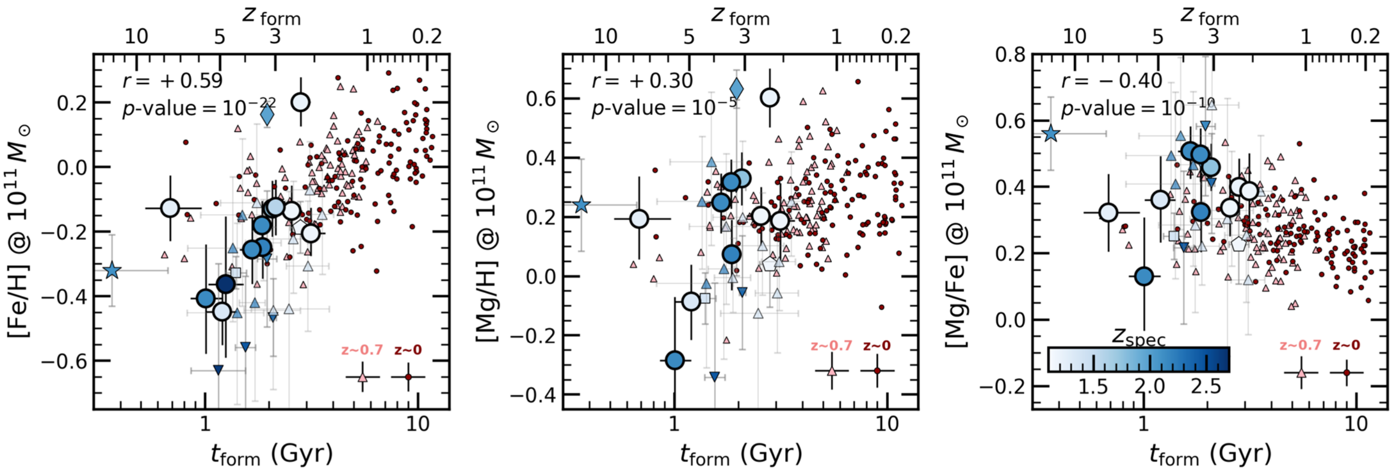

Figure 4. [Fe/H], [Mg/H], and [Mg/Fe] as a function of galaxy formation time for massive quiescent galaxies at $z = 0$–3. Data points for the redshift range $z = 1$–3 are color coded based on their spectroscopic redshift, and their shapes follow the same legend as Figure 2. The red circles [pink triangles] represent individual quiescent galaxies from SDSS [LEGA-C] (A. G. Beverage et al. 2023; Z. Zhuang et al. 2023). Typical uncertainties for the SDSS and LEGA-C points are shown in the bottom right of each panel. We remove the first-order dependence on stellar mass by adjusting all measurements to reflect the abundances at $M_* = 10^{11}\,M_\odot$ (refer to the text for details). We calculate the Pearson correlation coefficients, including all galaxies at all redshifts, and list the corresponding correlations (r) and p-values in the top left corner of each panel. Regardless of observed redshift, galaxies that form earlier have lower [Fe/H], slightly lower [Mg/H], and higher [Mg/Fe], consistent with more rapid formation and efficient quenching at earlier times.

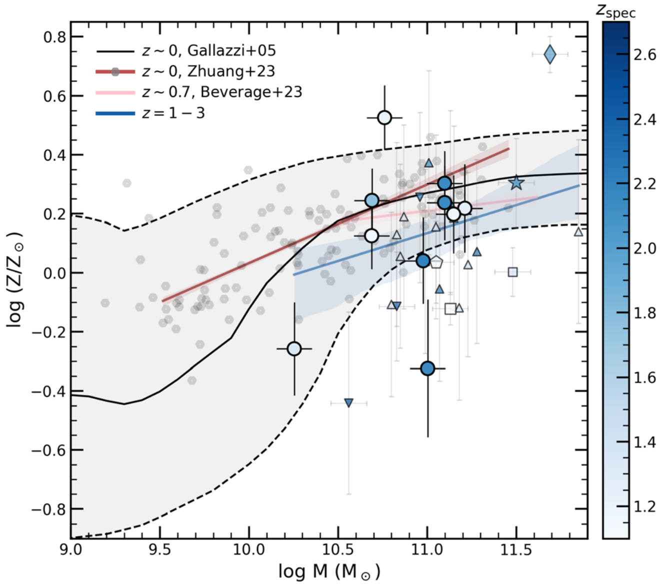

Figure 5. Stellar metallicity as a function of stellar mass for quiescent galaxies at $z = 1$–3 in the JWST-SUSPENSE program (circles) and from various other studies (following the same legend as Figure 2). All points are colored by their spectroscopic redshifts. The blue line shows the best-fit stellar MZR at $z = 1$–3, measured from all available measurements at $z = 1$–3. We include the stellar MZR at $z\sim0.7$ from A. G. Beverage et al. (2023, black dashed line) and $z\sim0$ from A. Gallazzi et al. (2005, black line and gray shaded region). We also show individual values from the SDSS sample presented in Z. Zhuang et al. (2023, gray hexagons). Galaxies $z = 1$–3 on average have -0.17 ± 0.09 dex lower metallicities than those at $z\sim0$ and $z\sim0.7$.

population modeling (see M. Kriek et al. 2016, for motivation of mass uncertainties). The best-fit parameters and corresponding uncertainties are estimated using MCMC. We use the same fitting method to redetermine the MZR at $z\sim0$ (red line) and $z\sim0.7$ (pink line) for the Z. Zhuang et al. (2023) and A. G. Beverage et al. (2023) samples, respectively. We emphasize again that the individual metallicity measurements at $z\sim0$ and $z\sim0.7$ were made using the same full-spectrum modeling method as the $z = 1$–3 sample.

The best-fit stellar MZRs at each redshift interval correspond to the following relations:

$z = 1$–3:

$$\log(Z/Z_\odot) = 0.19^{+0.17}_{-0.12}\log\left(\frac{M_*}{10^{11}\,M_\odot}\right) + 0.13^{+0.05}_{-0.11},$$

$z\sim0.7$:

$$\log(Z/Z_\odot) = 0.08^{+0.04}_{-0.04}\log\left(\frac{M_*}{10^{11}\,M_\odot}\right) + 0.21^{+0.02}_{-0.02},$$

$z\sim0$:

$$\log(Z/Z_\odot) = 0.27^{+0.02}_{-0.02}\log\left(\frac{M_*}{10^{11}\,M_\odot}\right) + 0.30^{+0.02}_{-0.02}.$$

The slope of the MZR at $z = 1$–3 is consistent with that at $z\sim0$, within the uncertainties. The normalization, though, appears to have increased by 0.17 ± 0.09 since $z\sim2$. We note that the sample at $z = 1$–3 is still small, and the metallicity measurements have significant statistical uncertainties. Consequently, the evidence for evolution remains below the 2σ level. Thus, larger samples and deeper observations are needed to confirm this potential evolution with more certainty.

An evolving MZR, if confirmed, is not surprising given that the total metal content of a galaxy is primarily in α elements (70%[20] by mass) and that we find slightly lower Mg in Figure 3. Even though distant quiescent galaxies are Fe deficient, Fe-peak elements only contribute 10% by mass to the total metallicity. Therefore, the observed offset in the MZR to lower $Z/Z_\odot$ could be explained by these galaxies having lower Mg abundances.

Other studies based on Lick indices instead point to a redshift-invariant MZR, with galaxies at $z\sim2$ having supersolar Z_* (I. Lonoce et al. 2015; M. Onodera et al. 2015). However, these conclusions are based on individual measurements or a single stacked spectrum, and therefore they carry

---

[20] Calculated using the M. Asplund et al. (2009) solar abundances and taking α elements to include N, O, Mg, Na, Ne, S, Si, Ti, and Ca.

large uncertainties. Similarly, V. Estrada-Carpenter et al. (2019) report a redshift-invariant MZR, with stellar metallicities derived from low-resolution spectroscopy. In Section 5.4, we compare these methods and demonstrate that metallicities derived from spectrophotometric fitting primarily reflect [Fe/H]. Given the Fe deficiencies found in this work, it is notable that V. Estrada-Carpenter et al. (2019) find no evolution in the MZR.

5. Discussion and Implications

5.1. Star Formation Timescales

In this work, we present the first abundance pattern study (including Fe, C, Mg, Si, Ca, and Ti) based on a sample of $z > 1$ quiescent galaxies. M. Jafariyazani et al. (2020) had previously measured an abundance pattern at $z \sim 2$, but only for a single lensed system, whereas A. G. Beverage et al. (2024) measured only the Mg and Fe abundances of a larger sample of quiescent galaxies at $z \sim 1.4$ and $z \sim 2.1$. In this section, we discuss the implication of multielement abundance results on the SFHs of distant quiescent galaxies.

A key observation from Figure 3 was that massive quiescent galaxies at $z = 1$–3 are deficient in Fe and C, whereas Mg, Si, Ca, and Ti have higher abundances. When considering the full interstellar medium (ISM) enrichment over a stellar population's lifetime, Fe is forged approximately equally in CC SNe and SNe Ia, whereas C is enriched approximately equally by CC SNe and low-mass AGB stars. The other elements, Mg, Si, Ca, and Ti, are all primarily α elements, produced in CC SNe. These processes enrich over a diverse set of timescales; exploding massive stars (CC SNe) eject α elements almost instantaneously after the commencement of star formation, swiftly incorporating them into subsequent stellar generations. Alternatively, low- to intermediate-mass stars enrich the ISM on a delayed timescale due to their longer lifespans. One mechanism is via SNe Ia, which typically eject Fe-peak elements (e.g., Cr and Fe) only after a time delay of $\sim$0.5–1 Gyr. The other mechanism is via AGB stars, which have even shorter delay times than SNe Ia, enriching primarily C (and N) as early as 50 Myr but with a typical delay of $\sim$250 Myr (e.g., S. Cristallo et al. 2011, 2015; R. Maiolino & F. Mannucci 2019; J. W. Johnson et al. 2023). Thus, galaxies that stop forming stars before significant AGB and SN Ia contributions have very low Fe-peak and C + N stellar abundances, but still high α abundances.

Considering the different enrichment timescales, our low C and Fe abundance results imply that the SUSPENSE galaxies formed most of their stellar mass before significant AGB and SN Ia enrichment, corresponding to a timescale of $\lesssim$0.2 Gyr. Such an extreme star formation timescale would translate to an SFR of $\geqslant 500\ M_\odot\ \mathrm{yr}^{-1}$, putting these galaxies among the most vigorous star-forming galaxies in the Universe (e.g., D. A. Riechers et al. 2013; R. Decarli et al. 2017; B. Gullberg et al. 2019; C.-L. Liao et al. 2024).

This interpretation assumes that the observed deficiencies in C and Fe are solely driven by shorter star formation timescales in higher-redshift galaxies. However, variations in the IMF may also play a significant role in shaping the relative elemental abundances. For instance, a top-heavy IMF would increase the relative number of CC SNe to SNe Ia, increasing the Mg producers over the Fe producers. This would elevate [Mg/Fe] without requiring extremely short star formation timescales (e.g., F. Matteucci 1994; D. Thomas et al. 1999). Furthermore, a top-heavy IMF could alter the IMF-averaged CC SN yields, introducing even more variation. A top-heavy IMF is indeed plausible in these extreme galaxies, potentially due to unique environmental conditions or the effect of an integrated galaxy-wide IMF (e.g., F. Fontanot et al. 2017). However, the extent of this impact—particularly on elements that are produced by multiple enrichment pathways—remains unclear. Detailed chemical evolution modeling is necessary to disentangle the respective roles of the IMF and star formation timescales in producing these unusual abundance patterns.

Such detailed chemical evolution models would also provide more precise estimates of star formation timescales, a task we leave for a future work. However, we note that the inferred extreme star formation timescales conflict with the results from spectrophotometric fitting using the nonparametric SFHs of the SUSPENSE galaxies M. Slob et al. (2024). In Sections 5.4 and 5.5 we discuss the implications of these differences.

5.2. The Assembly of Massive Galaxies over Cosmic Time

Our elemental abundance patterns imply that galaxies at $z \sim 2$ on average formed earlier (Section 3) and over shorter timescales (Section 5.1) compared to galaxies with similar velocity dispersions at $z \sim 0$ and $z \sim 0.7$. The most straightforward explanation for this observed increase is that galaxies in the quiescent sample at $z = 1$–3 are among the earliest quenchers in the $z \sim 0$ population; galaxies that form over longer timescales quench and join the quiescent galaxy population at later times. Thus, by $z = 0$, the SUSPENSE sample represents only the extreme tail of the t_{form} distribution. This explanation is akin to the "progenitor bias" scenario (i.e., P. G. van Dokkum & M. Franx 2001) used, for example, to explain the size growth of quiescent galaxies over time (e.g., S. Khochfar & J. Silk 2006; P. G. van Dokkum et al. 2010; C. M. Carollo et al. 2013; B. M. Poggianti et al. 2013).

This progenitor bias scenario is reinforced by Figure 4, where we find a negative correlation between formation time and [Mg/Fe], irrespective of the observed redshift of the galaxies. Thus, the evolution in C and Fe is mostly due to the lower-redshift samples naturally including galaxies with earlier formation times and shorter star formation timescales.

A closer look at Figure 4, however, reveals that progenitor bias alone may not be able to explain the observations. If the $z \sim 2$ galaxies passively evolve over the past 10 billion years, without merging or experiencing late-time star formation, then the trends with formation time at $z \sim 0$ and $z \sim 2$ should exactly overlap at the earliest epochs. Instead, we find very few SDSS galaxies at these early formation times and we find that the $z \sim 2$ samples exhibit slightly lower [Fe/H] and [Mg/H], and higher [Mg/Fe] than the lower-redshift samples. This offset was first identified by Z. Zhuang et al. (2023) using a small sample of objects at $z = 1$–3, and later confirmed by A. G. Beverage et al. (2024) with a larger sample.

One way to explain the lack of chemically extreme galaxies at $z \sim 0$ is late-time star formation episodes. If the star formation material is preenriched with SN Ia products by previous epochs of star formation, then the newly formed stars would be younger, more metal rich, and more α/Fe enhanced, pushing them along the abundance trends of Figure 4 toward younger ages (later formation times). Major mergers between galaxies with different SFHs would also shift galaxies upward along the formation time sequence. In contrast, minor mergers tend to decrease not only [Fe/H] but also [Mg/H] levels. However, due to aperture effects, interpreting the impact of minor mergers is more complicated because they are preferentially accreted onto the outskirts of galaxies. Therefore, minor mergers likely have minimal influence on the observed abundance patterns. Larger sample sizes at $z \gtrsim 1$ and $z \sim 0$ with careful consideration of stellar mass completeness are required to clarify the relative importance of progenitor bias, mergers, and late-time star formation.

5.3. *Galaxy Quenching*

A key finding from Figure 4 is galaxies that form at earlier epochs have lower [Mg/H]. Unlike the correlation with [Fe/H], this result cannot be explained using star formation timescales, because [Mg/H] instead reflects instantaneous enrichment by CC SNe.

One possible explanation for galaxies with earlier formation times having slightly lower [Mg/H] is that they expel larger gas reservoirs during the quenching phase. A. G. Beverage et al. (2021) proposed this model to explain a similar trend in the LEGA-C sample. They used a leaky box model with exponentially declining inflow rates and SN-driven outflows, with analytical solutions from E. Spitoni et al. (2017). In their models, galaxies with smooth SFHs that quench via slow gas depletion end up with high stellar [Mg/H] by $z = 0$, regardless of their SFH.

The implementation of rapid gas expulsion after two *e*-folding times (akin to AGN-driven feedback), successfully keeps the stellar [Mg/H] low. In these models, galaxies that quenched at higher SFR and thus expel larger gas reservoirs have lower [Mg/H] and earlier formation times. Thus, the observed correlation between [Mg/H] and $t_{\rm form}$ may indicate more efficient gas expulsion at higher redshift. These more efficient outflows in combination with progenitor bias, in turn, can explain the increase in [Mg/H] and the MZR over cosmic time.

This result, in combination with the extreme SFRs inferred from the C and Fe deficiencies, is consistent with quasar-driven quenching resulting from rapid gas inflows. Indeed, evidence of ejective AGN outflows has been found in galaxies that rapidly quenched after $z \sim 2$, indicated by pronounced blue-shifted Na I D and other ISM absorption lines (e.g., D. T. Maltby et al. 2019; M. Kubo et al. 2022; S. Belli et al. 2023; F. D'Eugenio et al. 2023; R. L. Davies et al. 2024; M. Park et al. 2024). Future chemical evolution modeling will help determine the mass-loading factors and star formation timescales required to reproduce the trends with $t_{\rm form}$.

5.4. *Stellar Population Synthesis Fitting*

In this section, we compare measurements derived in this work with those obtained using a more standard stellar population modeling approach, which employs solar abundance patterns and nonparametric SFHs. M. Slob et al. (2024) present stellar population parameters for the SUSPENSE galaxies using the PROSPECTOR code (J. Leja et al. 2019a; B. D. Johnson et al. 2021). PROSPECTOR utilizes the the Flexible Stellar Population Synthesis (C. Conroy et al. 2009; C. Conroy & J. E. Gunn 2010) library, the MILES spectral library, and the MIST isochrones, assuming a G. Chabrier (2003) IMF. The fitting process incorporates both JWST spectroscopy and UltraVISTA DR3 photometry. For more details, see M. Slob et al. (2024).

There are a few key differences between this standard modeling approach and the method used in this work. First, in PROSPECTOR and similar codes, such as BAGPIPES (A. C. Carnall et al. 2018), CIGALE (D. Burgarella et al. 2005), and MAGPHYS (E. da Cunha et al. 2008), the SFH is a free parameter. Second, they assume a solar-scaled abundance pattern (and sometimes $Z = Z_\odot$). Another key difference is that PROSPECTOR, when fitting both the photometry and spectra, heavily relies on the galaxy continuum shape and consequently does not put emphasis on reproducing the individual absorption features. In contrast, our full-spectrum modeling assumes a variable abundance pattern, a single burst of star formation, and relies solely on the stellar absorption features.

Before comparing the results from these codes, it is important to highlight that differences in the SFH assumptions lead to the derived quantities being either light-weighted values in PROSPECTOR or SSP-equivalent values in `alf`α. Thus, it is crucial to assess how these assumptions may impact the inferred properties. Recent work by N. M. Gountanis et al. (2024) tested the SSP assumption by generating composite spectra using a superposition of SSPs with evolving ages, metallicities, and abundance ratios [Mg/Fe], informed by a delayed-τ SFH and chemical evolution models. They then fit these composite spectra using `alf`α, assuming a single SSP. The results showed excellent agreement between the SSP-equivalent parameters and the true light-weighted averages, with discrepancies within 0.05 dex for ages, metallicities, and [Mg/Fe] (see their Figure 13). This test indicates that using an SSP-equivalent approach in `alf`α does not introduce significant biases, allowing for a valid comparison between the codes.

In Figure 6, we compare our best-fit ages and metallicities to those from PROSPECTOR. The points are colored by their spectroscopic redshift, and the dashed black lines represent the one-to-one line. The left panel shows stellar ages, where PROSPECTOR provides mass-weighted estimates and our full-spectrum fitting gives SSP-equivalent ages. Despite different assumptions in SFH (extended nonparametric versus single age), the two sets of stellar ages agree remarkably well. This result may not be surprising, as all of the galaxies in our sample have been quiescent for at least $\gtrsim$1 Gyr. At these older ages, these stellar populations are less susceptible to the outshining problem, wherein the youngest stars with low M/L dominate the continuum.

Next, we examine stellar metallicities in the middle panel of Figure 6, comparing $\log(Z/Z_\odot)$. As a reminder, the total metallicities from this work were computed using a combination of the best-fit [Mg/Fe] and [Fe/H]. We find poor agreement between our total metallicities and those from PROSPECTOR, with significant scatter (standard deviation = 0.32 dex) and a systematic offset of 0.41 dex toward lower values in the PROSPECTOR measurements. When we compare the PROSPECTOR metallicities instead to [Fe/H], the systematic offset disappears. However, the large scatter around the one-to-one line remains. Additionally, the uncertainties on the PROSPECTOR measurements are significantly underestimated.

The reason the PROSPECTOR $\log(Z/Z_\odot)$ aligns better with [Fe/H] rather than the total stellar metallicity is that Mg has less impact on the spectral shape compared to Fe (e.g., J. Choi et al. 2019; J. Leja et al. 2019b). As discussed in Section 4, despite Fe's significant contribution to the absorption features

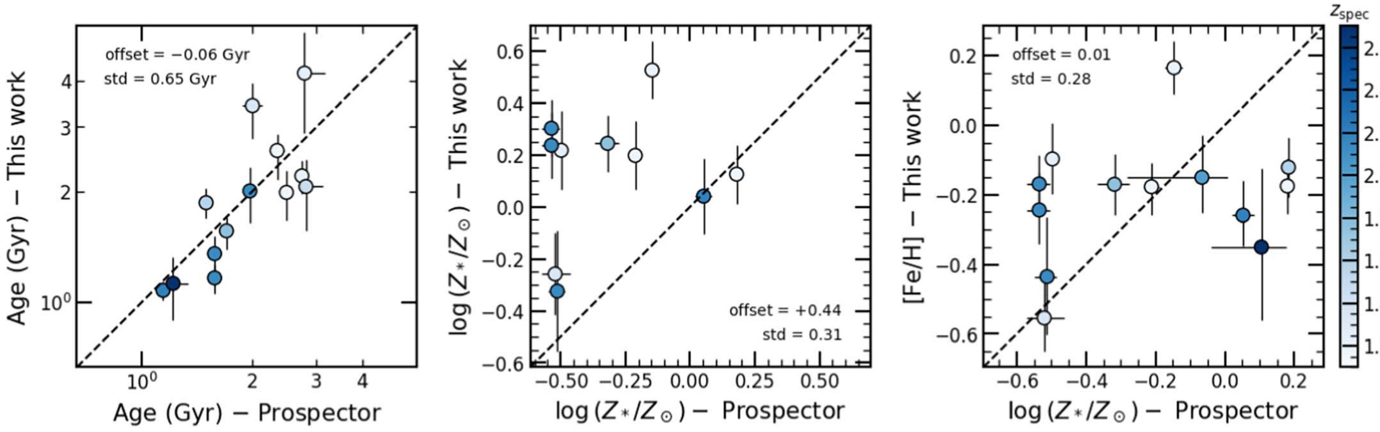

Figure 6. Comparison between PROSPECTOR and `alf`α measurements of the ages (left), metallicities (middle), and [Fe/H] (right) of the massive quiescent galaxies at $z = 1$–3 from JWST-SUSPENSE. The dashed black line shows the one-to-one relation. The data points are colored by their spectroscopic redshifts. The metallicities from this work are calculated using the D. Thomas et al. (2003) conversion to [Z/H] from [Fe/H] and [Mg/Fe]. The standard deviation of the points and mean offset are listed in each panel.

in galaxies, it contributes only a small fraction to the total metal content. This effect is even more pronounced in light of the Fe deficiencies found for the $z = 1$–3 sample.

The significant disagreement between the metallicities derived from PROSPECTOR and those presented here is surprising, especially given that both methods use nearly identical stellar population models (MIST isochrones and MILES stellar libraries). However, three key differences remain: PROSPECTOR incorporates photometry (capturing continuum shape), allows for an extended SFH, and uses a solar-scaled abundance pattern. To investigate the source of the discrepancy, we conducted the following tests. First, running PROSPECTOR on the continuum-normalized spectrum (excluding photometry) still showed a significant discrepancy with the results presented here, indicating the continuum shape is not the main cause. Second, constraining PROSPECTOR to an SSP to match `alf`α's SFH did not resolve the disagreement either. Finally, additionally forcing `alf`α to adopt a solar-scaled abundance pattern improved the metallicity agreement, though significant scatter remained. This final test was the only case where the metallicities from PROSPECTOR and `alf`α showed significant correlation according to the Pearson correlation test (p-value = 0.08). These results suggest that while multiple factors contribute, fitting nonsolar populations with solar-scaled abundance patterns significantly impacts the metallicity estimates.

This impact of assuming a solar-scaled abundance pattern when fitting α-enhanced galaxies is further demonstrated by the performance of PROSPECTOR's best-fit models, as shown in M. Slob et al. (2024). PROSPECTOR often struggles to reproduce key spectral features, particularly those associated with Mg, Si, and C, underscoring that solar-scaled models fail to capture the nonsolar abundances present in these galaxies. This finding is corroborated by the reduced χ^2 values from fitting the spectra with solar-scaled abundance patterns with `alf`α: solar-scaled fits result in a typical reduced χ^2 of 1.3, while allowing for nonsolar abundances improves the fit to 1.1.

Therefore, caution is needed when interpreting or assuming metallicities derived from codes using a solar abundance pattern. Such measurements often carry underestimated uncertainty, fail to trace the true metallicity, and, on average, are more likely to reflect the Fe abundance, which is a biased indicator of total metallicity.

Finally, we compare the best-fit SFHs from PROSPECTOR to those inferred from the elemental abundances. The typical star formation timescales from PROSPECTOR, which we define as $(t_{84} - t_{16})$,[21] is 1.2 Gyr, a factor of 6 longer than that predicted by the C and Fe deficiencies and chemical evolution arguments (∼200 Myr). It is perhaps not surprising that the SFHs derived from PROSPECTOR tend to be longer. At these stellar ages (1–4 Gyr), the time resolution of the stellar population synthesis models is only ∼1 Gyr (S. Zibetti et al. 2024), since the spectra of older stellar populations are less sensitive to changes in age. In contrast, the spectra of young quiescent galaxies are significantly more sensitive to age, and age resolution can be as low as ∼20 Myr (K. A. Suess et al. 2022b). This lower resolution in older stellar populations motivates future work that integrates stellar population modeling with priors informed by chemical evolution, which could help reveal the shorter star formation timescales we infer from chemical evolution arguments. These shorter timescales provide crucial insights into the buildup of massive galaxies, as discussed in the next section.

5.5. The Early Formation of Massive Galaxies

The short star formation timescales inferred from the abundance patterns may have broader implications for the formation of massive galaxies in the early Universe. Recently, JWST identified a population of quiescent and extremely massive galaxies at $z \gtrsim 3$ (J. Antwi-Danso et al. 2023; A. C. Carnall et al. 2024; A. de Graaff et al. 2024; K. Glazebrook et al. 2024; S. M. U. Stawinski et al. 2024). The SFHs of these galaxies, derived using PROSPECTOR and similar fitting codes, indicate that they begin to accumulate their stellar mass at very early epochs ($z \gtrsim 10$). It has been suggested that this early stellar mass growth may be in conflict with the predictions of ΛCDM, even when assuming a maximum (100%) baryon-to-star conversion efficiency, highlighting the "impossibly early galaxy problem" (e.g., C. Steinhardt et al. 2016).

One way to explain this tension is that the SFHs derived from standard modeling techniques are biased toward more extended SFHs. Most of the nonparametric SFHs were intentionally designed to include an early buildup of stellar

---

[21] Where t_x corresponds to the age of the Universe at which x percent of the stellar mass has been formed.

mass, to solve inconsistencies with lower-redshift galaxy evolution studies (A. C. Carnall et al. 2019, 2024; J. Leja et al. 2019a, 2019c). Therefore, these models may not apply to the $z \gtrsim 2$ galaxy population. A. C. Carnall et al. (2024) fitted an instantaneous burst of star formation to three massive quiescent galaxies at $z \gtrsim 3$. In this test, the best-fit stellar ages were consistent with the original fits; however, the initial buildup of stellar mass was delayed. These results show that these early massive galaxies could be explained within the ΛCDM framework by simply shortening the assumed SFHs.

Our elemental abundance results indeed show that standard stellar population modeling codes overestimate the duration of the star-forming phase. Thus, assuming that quiescent galaxies at $z > 3$ will have similarly short star formation timescales, the early mass buildup in these massive galaxies may be less problematic than found by earlier studies. As elemental abundance studies will be prohibitively difficult at $z > 3$, our elemental abundance pattern may help set more informative priors on the SFHs in stellar population modeling codes.

6. Summary

In this paper, we present the stellar metallicities and multielement abundances (C, Mg, Si, Ca, Ti, Cr, and Fe) of 15 massive quiescent galaxies at $z = 1$–3 from the JWST-SUSPENSE program. The ultradeep (16 hr) NIRSpec/MSA spectra were modeled using the custom full-spectrum fitting code `alfα`, a Python implementation of `alf` (C. Conroy et al. 2018), which has been made publicly available.

Compared to the $z \sim 0$ and $z \sim 0.7$ populations of massive quiescent galaxies, those at $z = 1$–3 have -0.26 ± 0.04 dex lower [C/H], -0.16 ± 0.03 dex lower [Fe/H], and -0.07 ± 0.04 dex lower [Mg/H]. There is also evidence that the quiescent MZR at $z = 1$–3 is lower by 0.17 ± 0.09 dex, but the uncertainties are large and the sample size is small. The C and Fe deficiencies indicate that distant quiescent galaxies form over shorter star formation timescales than today's quiescent galaxy population, quenching before significant enrichment by AGB stars and SNe Ia. Such rapid star formation timescales (∼0.2 Gyr) correspond to extreme SFRs of $\sim 500\ M_\odot\ \mathrm{yr}^{-1}$ at $z \sim 2$–10, putting these galaxies among the most vigorous star-forming galaxies in the Universe. In the future, chemical evolution modeling will offer more precise constraints on the star formation timescale, while also providing insights into the role of a top-heavy IMF in shaping this timescale.

We also find correlations between galaxy formation time and [Fe/H], [Mg/H], and [Mg/Fe], such that galaxies that form at earlier times have abundances consistent with shorter star formation timescales (i.e., higher [Mg/Fe] and lower [Fe/H]). These trends had previously been found within the $z \sim 0$ and $z \sim 0.7$ populations (A. G. Beverage et al. 2023; Z. Zhuang et al. 2023); however, using the $z = 1$–3 results, we show that the same trends extend to higher redshift and earlier formation times. This result suggests that the observed evolution in [C/H] and [Fe/H] over cosmic time is driven by lower-redshift samples naturally including galaxies that formed over longer timescales. In other words, the $z = 1$–3 quiescent galaxies represent the extreme tail of today's massive quiescent galaxy population. Interestingly, the $z \sim 0$ sample lacks the chemically extreme galaxies at $z = 1$–3, indicating mergers and/or late-time star formation likely contribute to the evolution in the elemental abundances. Larger sample sizes and careful consideration of completeness are required to clarify this picture.

Additionally, we confirm the marginal correlation between [Mg/H] and formation time suggested by previous results with smaller sample sizes and larger measurement uncertainties (Z. Zhuang et al. 2023; A. G. Beverage et al. 2024). Given that Mg is a tracer of instantaneous metal enrichment and not the star formation timescale, this marginal trend may imply that galaxies that form at earlier times expel larger gas reservoirs during the quenching phase, as suggested previously by A. G. Beverage et al. (2021). Combined with the extreme SFRs inferred from the C and Fe deficiencies, this interpretation is consistent with quenching by AGN-driven outflows. In the future, we will use chemical evolution modeling to measure the mass-loading factors and star formation timescales required to reproduce the trends with t_{form}.

Next, we compare our stellar ages and metallicities to results from the spectrophotometric modeling code PROSPECTOR, which assumes a solar-scaled elemental abundance pattern and a nonparametric SFH. The stellar ages agree remarkably well, but the stellar metallicities disagree significantly. Furthermore, the PROSPECTOR metallicities carry vastly underestimated uncertainties. However, despite the large scatter, the PROSPECTOR metallicities are in better agreement with [Fe/H], and not the total metal content [Z/H]. We attribute this result to solar-scaled models being more sensitive to [Fe/H] because of the strong impact of Fe on the stellar spectrum. Thus, although Fe only contributes approximately 10% by mass to the total metal content of quiescent galaxies, its abundance significantly impacts the optical stellar spectrum. In light of the observed Fe deficiencies and underestimated measurement uncertainties, we therefore emphasize caution when interpreting or assuming metallicities from modeling codes that adopt solar abundance patterns.

Finally, we find that the star formation timescales indicated by the extreme elemental abundance patterns of distant quiescent galaxies are significantly shorter than those predicted by standard spectrophotometric modeling codes. This discrepancy confirms that the SFHs from these codes may be overly biased toward extended and early stellar mass buildup when applied to distant quiescent galaxies (e.g., A. C. Carnall et al. 2019; J. Leja et al. 2019a, 2019c). Addressing this bias could help mitigate the possible tension with ΛCDM for quiescent galaxies at $z > 3$ (see also A. C. Carnall et al. 2024). As elemental abundance measurements become prohibitively challenging at $z > 3$, these findings demonstrate how our elemental abundance patterns can provide more informative priors on the SFHs in stellar population modeling codes.

In this paper, we demonstrate the power of JWST for studying the multielement abundances of distant quiescent galaxies. In the future, we will combine this expanding multielement data set at $z \gtrsim 1$ with chemical evolution modeling, to uncover a more detailed picture of the SFHs, quenching, and assembly of massive quiescent galaxies over cosmic time.

Acknowledgments

This work is based on observations made with the NASA/ESA/CSA James Webb Space Telescope. The data were obtained from the Mikulski Archive for Space Telescopes at the Space Telescope Science Institute, which is operated by the Association of Universities for Research in Astronomy, Inc., under NASA contract NAS 5-03127 for JWST. These observations are associated with program JWST-GO-2110. Support for program JWST-GO-2110 was provided by NASA through a grant from the Space Telescope Science Institute, which is operated by the Association of Universities for Research in Astronomy, Inc., under NASA contract NAS 5-03127. A.G.B. is supported by the National Science Foundation Graduate Research Fellowship Program under grant Nos. DGE 1752814 and DGE 2146752 and by the H2H8 Association and Leids Kerkhoven-Bosscha Fonds. M.K. acknowledges funding from the Dutch Research Council (NWO) through the award of the Vici grant VI.C.222.047 (project 2010007169). C. C. acknowledges support from NSF Award 1908748.

The JWST data presented in this article were obtained from the Mikulski Archive for Space Telescopes (MAST) at the Space Telescope Science Institute. The specific observations analyzed can be accessed via doi:10.17909/6wjp-qb35.

Facility: JWST (NIRSpec).

Software: PROSPECTOR (J. Leja et al. 2019a; B. D. Johnson et al. 2021), `alf` (C. Conroy & P. van Dokkum 2012; C. Conroy et al. 2018), and `alf`α.

Appendix
Tables of Elemental Abundance Ratios

In this appendix, we present tables of the abundance ratios [X/Mg] (Table 2) and [X/Fe] (Table 3) of the SUSPENSE galaxies. The uncertainties are derived from the MCMC chains, which account for potential non-Gaussianity in the posterior distributions of the absolute abundances, [X/H].

Table 2
Elemental Abundance Ratios with Mg as the Reference Element

ID	[Fe/Mg]	[C/Mg]	[Ca/Mg]	[Ti/Mg]	[Cr/Mg]	[Si/Mg]
127345	$-0.32^{+0.09}_{-0.09}$	$-0.17^{+0.11}_{-0.12}$	$-0.00^{+0.10}_{-0.10}$	…	$-0.33^{+0.13}_{-0.12}$	$-0.24^{+0.15}_{-0.16}$
130040	$-0.40^{+0.12}_{-0.11}$	$-0.16^{+0.16}_{-0.17}$	$-0.26^{+0.12}_{-0.12}$	$0.15^{+0.18}_{-0.20}$	$-0.19^{+0.16}_{-0.16}$	$-0.29^{+0.18}_{-0.17}$
127154	$-0.38^{+0.08}_{-0.08}$	$-0.26^{+0.11}_{-0.11}$	…	$-0.08^{+0.14}_{-0.16}$	$-0.49^{+0.14}_{-0.14}$	$-0.17^{+0.14}_{-0.14}$
129982	$-0.34^{+0.12}_{-0.12}$	$-0.29^{+0.18}_{-0.17}$	$-0.21^{+0.16}_{-0.17}$	$-0.18^{+0.20}_{-0.19}$	$-0.04^{+0.16}_{-0.16}$	…
127108	$-0.32^{+0.13}_{-0.13}$	$-0.54^{+0.18}_{-0.17}$	$-0.36^{+0.21}_{-0.21}$	…	$-0.70^{+0.18}_{-0.18}$	$0.01^{+0.23}_{-0.28}$
129197	…	…	…	…	…	…
129149	…	…	…	…	…	…
128041	$-0.44^{+0.07}_{-0.07}$	$-0.45^{+0.09}_{-0.09}$	$-0.39^{+0.07}_{-0.07}$	$-0.11^{+0.12}_{-0.13}$	$-0.54^{+0.11}_{-0.11}$	$-0.49^{+0.14}_{-0.14}$
127700	…	…	…	…	…	…
129133	$-0.51^{+0.08}_{-0.07}$	$-0.29^{+0.10}_{-0.10}$	$-0.08^{+0.08}_{-0.09}$	…	$-0.47^{+0.15}_{-0.15}$	$-0.27^{+0.18}_{-0.20}$
129133	$-0.50^{+0.08}_{-0.08}$	$-0.32^{+0.09}_{-0.09}$	$-0.11^{+0.09}_{-0.08}$	…	$-0.47^{+0.14}_{-0.13}$	$-0.26^{+0.17}_{-0.18}$
127941	$-0.12^{+0.16}_{-0.18}$	$-0.16^{+0.19}_{-0.20}$	$0.51^{+0.16}_{-0.17}$	…	$0.39^{+0.20}_{-0.22}$	$0.32^{+0.24}_{-0.27}$
128036	$-0.32^{+0.12}_{-0.12}$	$-0.33^{+0.13}_{-0.13}$	$0.09^{+0.12}_{-0.12}$	…	$-0.51^{+0.19}_{-0.18}$	$-0.31^{+0.22}_{-0.23}$
128913	…	…	…	…	…	…
130725	…	…	…	…	…	…
129966	…	…	…	…	…	…

Table 3
Elemental Abundance Ratios with Fe as the Reference Element

ID	[Mg/Fe]	[C/Fe]	[Ca/Fe]	[Ti/Fe]	[Cr/Fe]	[Si/Fe]
127345	$0.32^{+0.09}_{-0.09}$	$0.15^{+0.10}_{-0.10}$	$0.32^{+0.09}_{-0.09}$	…	$-0.01^{+0.12}_{-0.12}$	$0.08^{+0.13}_{-0.14}$
130040	$0.40^{+0.11}_{-0.12}$	$0.24^{+0.13}_{-0.14}$	$0.14^{+0.10}_{-0.10}$	$0.55^{+0.20}_{-0.23}$	$0.21^{+0.16}_{-0.16}$	$0.11^{+0.15}_{-0.14}$
127154	$0.38^{+0.08}_{-0.08}$	$0.13^{+0.09}_{-0.10}$	…	$0.31^{+0.14}_{-0.17}$	$-0.10^{+0.13}_{-0.14}$	$0.22^{+0.12}_{-0.13}$
129982	$0.34^{+0.12}_{-0.12}$	$0.05^{+0.16}_{-0.16}$	$0.13^{+0.15}_{-0.15}$	$0.16^{+0.21}_{-0.22}$	$0.29^{+0.16}_{-0.16}$	…
127108	$0.32^{+0.13}_{-0.13}$	$-0.22^{+0.14}_{-0.14}$	$-0.05^{+0.20}_{-0.19}$	…	$-0.40^{+0.15}_{-0.14}$	$0.32^{+0.19}_{-0.24}$
129197	…	…	…	…	…	…
129149	…	$0.13^{+0.10}_{-0.09}$	$-0.07^{+0.08}_{-0.08}$	$0.35^{+0.16}_{-0.18}$	$0.18^{+0.16}_{-0.15}$	$0.12^{+0.16}_{-0.18}$
128041	$0.44^{+0.07}_{-0.07}$	$-0.01^{+0.08}_{-0.08}$	$0.05^{+0.06}_{-0.06}$	$0.34^{+0.12}_{-0.13}$	$-0.10^{+0.11}_{-0.11}$	$-0.05^{+0.12}_{-0.13}$
127700	…	$-0.08^{+0.15}_{-0.15}$	$-0.02^{+0.13}_{-0.12}$	…	…	…
129133	$0.51^{+0.07}_{-0.08}$	$0.22^{+0.11}_{-0.10}$	$0.42^{+0.08}_{-0.08}$	…	$0.04^{+0.15}_{-0.14}$	$0.24^{+0.17}_{-0.20}$
129133	$0.50^{+0.08}_{-0.08}$	$0.18^{+0.09}_{-0.09}$	$0.39^{+0.08}_{-0.07}$	…	$0.03^{+0.14}_{-0.13}$	$0.24^{+0.16}_{-0.17}$
127941	$0.12^{+0.18}_{-0.16}$	$-0.04^{+0.17}_{-0.17}$	$0.62^{+0.12}_{-0.12}$	…	$0.51^{+0.18}_{-0.21}$	$0.44^{+0.21}_{-0.24}$
128036	$0.32^{+0.12}_{-0.12}$	$-0.01^{+0.11}_{-0.12}$	$0.41^{+0.09}_{-0.09}$	…	$-0.19^{+0.19}_{-0.18}$	$0.01^{+0.19}_{-0.21}$
128913	…	…	…	…	…	…
130725	…	…	$0.26^{+0.20}_{-0.20}$	…	…	…
129966	…	…	…	…	…	…

ORCID iDs

Aliza G. Beverage https://orcid.org/0000-0002-9861-4515
Martje Slob https://orcid.org/0000-0001-7540-1544
Mariska Kriek https://orcid.org/0000-0002-7613-9872
Charlie Conroy https://orcid.org/0000-0002-1590-8551
Guillermo Barro https://orcid.org/0000-0001-6813-875X
Rachel Bezanson https://orcid.org/0000-0001-5063-8254
Gabriel Brammer https://orcid.org/0000-0003-2680-005X
Chloe M. Cheng https://orcid.org/0000-0003-2251-9164
Anna de Graaff https://orcid.org/0000-0002-2380-9801
Natascha M. Förster Schreiber https://orcid.org/0000-0003-4264-3381
Marijn Franx https://orcid.org/0000-0002-8871-3026
Brian Lorenz https://orcid.org/0000-0002-5337-5856
Pavel E. Mancera Piña https://orcid.org/0000-0001-5175-939X
Danilo Marchesini https://orcid.org/0000-0001-9002-3502
Adam Muzzin https://orcid.org/0000-0002-9330-9108
Andrew B. Newman https://orcid.org/0000-0001-7769-8660
Sedona H. Price https://orcid.org/0000-0002-0108-4176
Alice E. Shapley https://orcid.org/0000-0003-3509-4855
Mauro Stefanon https://orcid.org/0000-0001-7768-5309
Katherine A. Suess https://orcid.org/0000-0002-1714-1905
Pieter van Dokkum https://orcid.org/0000-0002-8282-9888
David Weinberg https://orcid.org/0000-0002-6442-6030
Daniel R. Weisz https://orcid.org/0000-0002-6442-6030

References

Akhshik, M., Whitaker, K. E., Leja, J., et al. 2023, ApJ, 943, 179
Antwi-Danso, J., Papovich, C., Esdaile, J., et al. 2025, ApJ, 978, 90
Asplund, M., Grevesse, N., Sauval, A. J., & Scott, P. 2009, ARA&A, 47, 481
Barone, T. M., D'Eugenio, F., Scott, N., et al. 2022, MNRAS, 512, 3828
Belli, S., Park, M., Davies, R. L., et al. 2024, Natur, 630, 54
Beverage, A. 2024, alfalpha: A Python Adaptation of the 'alf' Code for Spectroscopic Modeling of Stellar Populations, v1, Zenodo, doi:10.5281/ZENODO.13882725
Beverage, A. G., Kriek, M., Conroy, C., et al. 2021, ApJL, 917, L1
Beverage, A. G., Kriek, M., Conroy, C., et al. 2023, ApJ, 948, 140
Beverage, A. G., Kriek, M., Suess, K. A., et al. 2024, ApJ, 966, 234
Burgarella, D., Buat, V., & Iglesias-Paramo, J. 2005, MNRAS, 360, 1413
Bushouse, H., Eisenhamer, J., Dencheva, N., et al. 2023, JWST Calibration Pipeline, v1.12.5, Zenodo, doi:10.5281/zenodo.10022973
Carnall, A. C., Cullen, F., McLure, R. J., et al. 2024, MNRAS, 534, 325
Carnall, A. C., Leja, J., Johnson, B. D., et al. 2019, ApJ, 873, 44
Carnall, A. C., McLure, R. J., Dunlop, J. S., & Dave, R. 2018, MNRAS, 480, 4379
Carnall, A. C., McLure, R. J., Dunlop, J. S., et al. 2022, ApJ, 929, 131
Carollo, C. M., Bschorr, T. J., Renzini, A., et al. 2013, ApJ, 773, 112
Chabrier, G. 2003, PASP, 115, 763
Choi, J., Conroy, C., & Johnson, B. D. 2019, ApJ, 872, 136
Choi, J., Conroy, C., Moustakas, J., et al. 2014, ApJ, 792, 95
Choi, J., Dotter, A., Conroy, C., et al. 2016, ApJ, 823, 102
Conroy, C., Graves, G. J., & van Dokkum, P. G. 2014, ApJ, 780, 33
Conroy, C., & Gunn, J. E. 2010, ApJ, 712, 833
Conroy, C., Gunn, J. E., & White, M. 2009, ApJ, 699, 486
Conroy, C., & van Dokkum, P. 2012, ApJ, 747, 69
Conroy, C., Villaume, A., Dokkum, P. G. v., & Lind, K. 2018, ApJ, 854, 139
Cristallo, S., Piersanti, L., Straniero, O., et al. 2011, ApJS, 197, 17
Cristallo, S., Straniero, O., Piersanti, L., & Gobrecht, D. 2015, ApJS, 219, 40
Curti, M., Maiolino, R., Curtis-Lake, E., et al. 2024, A&A, 684, A75
da Cunha, E., Charlot, S., & Elbaz, D. 2008, MNRAS, 388, 1595
Davies, R. L., Belli, S., Park, M., et al. 2024, MNRAS, 528, 4976
de Graaff, A., Rix, H.-W., Carniani, S., et al. 2024, A&A, 684, A87
de Graaff, A., Setton, D. J., Brammer, G., et al. 2024, NatAs, In press
Decarli, R., Walter, F., Venemans, B. P., et al. 2017, Natur, 545, 457
D'Eugenio, F., Perez-Gonzalez, P., Maiolino, R., et al. 2024, NatAs, 8, 1443
Estrada-Carpenter, V., Papovich, C., Momcheva, I., et al. 2019, ApJ, 870, 133
Fontanot, F., De Lucia, G., Hirschmann, M., et al. 2017, MNRAS, 464, 3812
Gallazzi, A., Bell, E. F., Zibetti, S., Brinchmann, J., & Kelson, D. D. 2014, ApJ, 788, 72
Gallazzi, A., Charlot, S., Brinchmann, J., White, S. D. M., & Tremonti, C. A. 2005, MNRAS, 362, 41
Glazebrook, K., Nanayakkara, T., Schreiber, C., et al. 2024, Natur, 628, 277
Gountanis, N. M., Weinberg, D. H., Beverage, A. G., et al. 2024, arXiv:2407.07971
Gullberg, B., Smail, I., Swinbank, A. M., et al. 2019, MNRAS, 490, 4956
Jafariyazani, M., Newman, A. B., Mobasher, B., et al. 2020, ApJ, 897, L42
Jafariyazani, M., Newman, A. B., Mobasher, B., et al. 2024, arXiv:2406.03549
Johnson, B. D., Leja, J., Conroy, C., & Speagle, J. S. 2021, ApJS, 254, 22
Johnson, J. W., Weinberg, D. H., Vincenzo, F., Bird, J. C., & Griffith, E. J. 2023, MNRAS, 520, 782
Khochfar, S., & Silk, J. 2006, ApJ, 648, L21
Kirby, E. N., Cohen, J. G., Guhathakurta, P., et al. 2013, ApJ, 779, 102
Kobayashi, C., Karakas, A. I., & Lugaro, M. 2020, ApJ, 900, 179
Kriek, M., Beverage, A. G., Price, S. H., et al. 2024, ApJ, 966, 36
Kriek, M., Conroy, C., van Dokkum, P. G., et al. 2016, Natur, 540, 248
Kriek, M., Price, S. H., Conroy, C., et al. 2019, ApJ, 880, L31
Kroupa, P. 2001, MNRAS, 322, 231
Kubo, M., Umehata, H., Matsuda, Y., et al. 2022, ApJ, 935, 89
Langeroodi, D., Hjorth, J., Chen, W., et al. 2023, ApJ, 957, 39
Leja, J., Carnall, A. C., Johnson, B. D., Conroy, C., & Speagle, J. S. 2019a, ApJ, 876, 3
Leja, J., Johnson, B. D., Conroy, C., et al. 2019b, ApJ, 877, 140
Leja, J., Tacchella, S., & Conroy, C. 2019c, ApJ, 880, L9
Lequeux, J., Peimbert, M., Rayo, J., Serrano, A., & Torres-Peimbert, S. 1979, A&A, 80, 145
Liao, C.-L., Chen, C.-C., Wang, W.-H., et al. 2024, ApJ, 961, 226
Lonoce, I., Longhetti, M., Maraston, C., et al. 2015, MNRAS, 454, 3912
Maiolino, R., & Mannucci, F. 2019, A&ARv, 27, 3
Maiolino, R., Nagao, T., Grazian, A., et al. 2008, A&A, 488, 463
Maltby, D. T., Almaini, O., McLure, R. J., et al. 2019, MNRAS, 489, 1139
Man, A. W. S., Zabl, J., Brammer, G. B., et al. 2021, ApJ, 919, 20
Maoz, D., Sharon, K., & Gal-Yam, A. 2010, ApJ, 722, 1879
Matteucci F. 1994, A&A, 288, 57
Morishita, T., Abramson, L. E., Treu, T., et al. 2018, ApJ, 856, L4
Muzzin, A., Marchesini, D., Stefanon, M., et al. 2013a, ApJS, 206, 8
Muzzin, A., Marchesini, D., Stefanon, M., et al. 2013b, ApJ, 777, 18
Nakajima, K., Ouchi, M., Isobe, Y., et al. 2023, ApJS, 269, 33
Onodera, M., Carollo, C. M., Renzini, A., et al. 2015, ApJ, 808, 161
Papovich, C., Simons, R. C., Estrada-Carpenter, V., et al. 2022, ApJ, 937, 22
Park, M., Belli, S., Conroy, C., et al. 2024, ApJ, 976, 72
Poggianti, B. M., Moretti, A., Calvi, R., et al. 2013, ApJ, 777, 125
Riechers, D. A., Bradford, C. M., Clements, D. L., et al. 2013, Natur, 496, 329
Sanchez-Blazquez, P., Peletier, R. F., Jimenez-Vicente, J., et al. 2006, MNRAS, 371, 703
Sanders, R. L., Shapley, A. E., Jones, T., et al. 2021, ApJ, 914, 19
Sanders, R. L., Shapley, A. E., Reddy, N. A., et al. 2020, MNRAS, 491, 1427
Saracco, P., Barbera, F. L., De Propris, R., et al. 2023, MNRAS, 520, 3027
Shapley, A. E., Reddy, N. A., Sanders, R. L., Topping, M. W., & Brammer, G. B. 2023, ApJL, 950, L1
Slob, M., Kriek, M., Beverage, A. G., et al. 2024, ApJ, 973, 131
Speagle, J. S. 2020, MNRAS, 493, 3132
Spitoni, E., Vincenzo, F., & Matteucci, F. 2017, A&A, 599, A6
Stawinski, S. M. U., Cooper, M. C., Forrest, B., et al. 2024, OJAp, 7, 46
Steinhardt, C., Capak, P., Masters, D., & Speagle, J. S. 2016, ApJ, 824, 21
Suess, K. A., Kriek, M., Bezanson, R., et al. 2022a, ApJ, 926, 89
Suess, K. A., Leja, J., Johnson, B. D., et al. 2022b, ApJ, 935, 146
Thomas, D., Greggio, L., & Bender, R. 1999, MNRAS, 302, 537
Thomas, D., Maraston, C., & Bender, R. 2003, MNRAS, 339, 897
Tremonti, C. A., Heckman, T. M., Kauffmann, G., et al. 2004, ApJ, 613, 898
van Dokkum, P. G., & Franx, M. 2001, ApJ, 553, 90
van Dokkum, P. G., Whitaker, K. E., Brammer, G., et al. 2010, ApJ, 709, 1018
Villaume, A., Conroy, C., Johnson, B., et al. 2017, ApJS, 230, 23
Weinberg, D. H., Holtzman, J. A., Hasselquist, S., et al. 2019, ApJ, 874, 102
Zahid, H. J., Geller, M. J., Kewley, L. J., et al. 2013, ApJ, 771, L19
Zhuang, Z., Leethochawalit, N., Kirby, E. N., et al. 2023, ApJ, 948, 132
Zibetti, S., Rossi, E., & Gallazzi, A. R. 2024, MNRAS, 528, 2790